MEAN GRAIN SIZE ESTIMATION FOR COPPER-ALLOY SAMPLES BASED ON ATTENUATION COEFFICIENT ESTIMATES

A Thesis presented to
the Faculty of the Graduate School
University of Missouri

In Partial Fulfillment
of the Requirements for the Degree

Master of Science in Mechanical and Aerospace Engineering

---

by
JOHN WILLIAM WAGNER

Dr. Steven P. Neal, Thesis Supervisor

DECEMBER 2011

The undersigned, appointed by the Dean of the Graduate School, have examined the thesis entitled

MEAN GRAIN SIZE ESTIMATION FOR COPPER-ALLOY SAMPLES BASED ON ATTENUATION COEFFICIENT ESTIMATES

Presented by John William Wagner

A candidate for the degree of Master of Science, Mechanical and Aerospace Engineering

And herby certify that in their opinion it is worthy of acceptance.

Dr. Steven P. Neal

Dr. Robert A. Winholtz

Dr. Glenn A. Washer

ACKNOWLEDGEMENTS

I owe great thanks to my advisor Dr. Steven P. Neal for supporting me throughout my undergraduate and graduate career at the University of Missouri. He has been a great mentor who has provided me with invaluable insight and direction for this research. Moreover, his mentorship has helped me foster skill sets which I will undoubtedly use throughout the rest of my engineering career.

I would like to thank the International Copper Association and the Wieland Group – Germany for supporting this research. I would like to thank the College of Mechanical and Aerospace Engineering for monetarily supporting me during my graduate studies at the University of Missouri. Finally, I would like to thank Dr. Winholtz and Dr. Washer for serving on my thesis committee.

Last, but most definitely not least: To my mom and dad, you have always been there to support me. You have taught me to always put my best foot forward and to never give up, regardless of how difficult a situation may be. Your relationship exemplifies the epitome of love. I hope that one day I can be half the role model to my children as you were both to me. I love you both. To my brother, you will always be my best friend. Your focus and determination have, and always will provide inspiration for my own pursuits in life. Your ambition will take you and those around you far. I love you.

TABLE OF CONTENTS

CHAPTER

2) Theoretical Basis

3) Experimental Set Up and Procedures

4) Signal Processing and Analysis

LIST OF ILLUSTRATIONS

Table Page

Figure

MEAN GRAIN SIZE ESTIMATION FOR COPPER-ALLOY SAMPLES BASED ON ATTENUATION COEFFICIENT ESTIMATES

John William Wagner

Dr. Steven P. Neal, Thesis Supervisor

ABSTRACT

A polycrystalline metal's grain size affects its mechanical properties; therefore, the ability to effectively and easily monitor grain size during a manufacturing process is critical. Conventional destructive tests utilized for estimating grain size or mechanical properties are expensive and time consuming. Past research has shown some success in nondestructively estimating a metal's mean grain size using attenuation coefficient measurements acquired from ultrasound. Within this research, a water immersion, pulse-echo mode of ultrasonic testing is employed to estimate the mean grain diameter of 5 thin copper-alloy samples using attenuation coefficient measurements. The attenuation coefficients were estimated via spectral analysis of interface reflections. The interface reflections were corrected for reflection and transmission effects, beam field diffraction, and water attenuation effects. An experimental diffraction correction approach and an inverse water attenuation filter accounted for diffraction and water attenuation, respectively. A Leave-One-Out (LOO) cross-validation algorithm was implemented to generate correlation models needed for grain diameter estimation. Models were developed as a function of ultrasonic wavelength and yielded grain diameter estimates for each sample. Estimates were seen to compare favorably with the stated grain diameters of the copper-alloy samples. This research was supported by the International Copper Association. Copper-alloy samples were supplied by the Wieland Group - Germany.

CHAPTER 1

Introduction

The capability to control and maintain specific production parameters for any manufacturing process has always been an issue of utmost importance within industry. Inherent to any production part, the part's material properties and/or design tolerances become a function of the manufacturing process utilized for its fabrication. Over the past 2 decades, nondestructive testing methods have become more powerful in their ability to evaluate whether or not a production part has deviated from its intended properties.

Within the nondestructive testing community, ultrasonic testing has long been considered the conventional method for industrial quality control. Ultrasonic testing is able to provide an effective tool in evaluating a material for microstructural flaws. Of no less importance, ultrasonic testing is highly sensitive to deviations in a material's microstructural properties [1]. For this reason, ultrasonic testing is often utilized for material characterization.

It has been well known that a material's microstructural properties greatly affect its mechanical properties; therefore, the ability to evaluate any changes occurring with a material' properties during a manufacturing process is extremely critical. A prime quality control example, which provides the motivation for this thesis, is estimating a polycrystalline metal's mean grain diameter. Grain size is a microstructural property that significantly affects a material's yield stress and fracture toughness [2]. A metal's grain size is a function of its fabrication process. Since a deviation in a process parameter could potentially change the grain structure of the metal, having the ability to evaluate any sample of interest without destructively examining it is highly advantageous.

There has been much work previously done in evaluating a material's grain structure via ultrasonics, and it is readily accepted that there exists a correlation between the amount of attenuation incurred within a polycrystalline metal and the metal's mean grain diameter. For this reason, ultrasonic testing is a method which readily lends itself towards metallurgical quality control.

This thesis documents research which utilized a water immersion mode, pulse-echo form of ultrasonic testing to estimate the mean grain diameter of 5 copper-alloy samples of plate type-geometry. These samples consisted of varying thicknesses, material compositions, and mean grain diameters. Furthermore, these samples were relatively thin, requiring considerable attenuation detection sensitivity.

Copper-alloys represent a materials group which is very prevalent in fluid transfer systems, such as high-pressure steam pipes, water mains, etc. During initial production, maintaining the intended grain size for a particular alloy within a given production run is essential for providing the required mechanical strength. Although the grain diameter of a single sample can be determined via conventional methods (e.g. optical microscopy), the amount of time and labor required to obtain this information is involved. Beyond this though, obtaining the mean grain diameter of many samples can be impractical, as each sample needs to be polished, etched, and then physically examined. The ability to utilize ultrasonic testing for estimating the mean grain diameter of relatively thin copper-alloy samples would provide for an even more robust metallurgical quality control method within industry.

As was previously mentioned, there has been significant interest in grain size evaluation via ultrasonics. Rayleigh was the very first to propose the idea of sound being scattered by localized foreign bodies within a matrix [3]. This idea was carried further by Mason and McSkimin who claimed that individual grains within a metal could be treated as localized foreign bodies. The successors of these pioneers formulated the explicit details of the currently accepted ultrasonic grain scattering theory. This theory states that there are 3 different scattering regimes, where each regime's expected degree of attenuation is dictated by the ratio of the acoustic wave's wavelength to that of the mean grain diameter of the propagation material.

Attenuation is a commonly used metric within ultrasonics. The attenuation incurred by a propagating wave front describes the amount of energy lost as the wave travels through its propagation medium. Many consider the amount of energy lost within polycrystalline materials such as metals to be predominantly attributed to scattering from the grains [4]. The grains scatter the propagating wave front through their grain boundaries, as these boundaries enable each grain to behave as a localized foreign body.

To date, the majority of ultrasonic grain size estimation approaches have been attenuation measurement methods utilizing a through transmission or pulse-echo mode of testing. Many early studies were aimed at observing the correlation between particular material characteristics of interest and the amount of attenuation incurred over remnant back surface reflections solely within the time domain. More recent attenuation methods have been focused on observing the amount of attenuation at a particular depth or frequency [5].

The work documented within this thesis observed the attenuation coefficient via spectral analysis, that is, within the frequency domain. Furthermore, the attenuation coefficient was isolated as a function of wavelength, as the correlation between mean grain diameter and the degree of attenuation is dependent upon the acoustic wavelength relative to the point of inhomogeneity.

The ultrasonic testing employed within this work utilized a focused, piezoelectric transducer. Signals were acquired through axial scans, that is, the transducer was incremented along the Z-axis towards the submersed sample. The attenuation data obtained from the as-measured signals was arrived to after extensive signal processing. The acquired signals were corrected for diffraction, water attenuation, and reflection and transmission effects. Diffraction correction was carried out using an Experimental Diffraction Correction (EDC) approach. Signal acquisition using axial scans advocated the EDC approach by allowing for diffraction curve analysis; however, each voltage-time signal (A-scan) was acquired at a different water path, requiring correction for varying water attenuation effects. A software-based water attenuation filter was used for this needed correction. The wave speed of each sample and density of each material was needed to estimate the reflection coefficient. Sample density was considered a priori knowledge. Each sample’s wave speed was experimentally calculated through measurement of the sample thickness and sample propagation time, that is, the time-of-flight. After the interface reflections were passed through the above correction factors, the sample’s attenuation coefficient was estimated. The estimation method utilized frequency domain regression fits applied to the front surface reflection (FSR), first back surface reflection (BSR1), fifth back surface reflection (BSR5), and sixth back surface reflection’s (BSR6) diffraction curves. The obtained attenuation coefficient data was then observed as a function of wavelength. Furthermore, the attenuation data was examined using a unique set of parameters within a selected wavelength regime of interest.

Attenuation-grain diameter correlation plots were developed from these parameters, and linear regressions were applied. The regressions were developed using a conventional cross-validation algorithm, commonly referred to as the Leave-One-Out (LOO) algorithm. This algorithm was utilized for grain diameter estimation. The supplied mean grain diameters of each sample were used as the reference for establishment of the LOO's estimation accuracy [6].

This thesis provides the theoretical background for the grain diameter estimation method implemented within this work and documents the application of the approach to a set of 5 thin copper-alloy samples. Chapter 2 of this thesis will present the basis for experimental diffraction correction, water attenuation correction, reflection and transmission effects correction, and the frequency domain beam models for which these correction factors were applied. Chapter 3 will follow with details regarding the experimental setup and experimental procedures. Chapter 4 will outline the software algorithm employed for signal processing and analysis needed for grain diameter estimation. Chapter 5 presents the grain diameter estimation results for the copper alloy samples, as obtained with the LOO algorithm. The final chapter will close with a summary and brief discussion.

CHAPTER 2

Theoretical Basis

2.1 Diffraction Fields and Equal Diffraction Points

In order to isolate the solid attenuation effects, that is, attenuation due to scattering from the sample, several correction factors were placed upon the beam models. These corrections factors accounted for the effects associated with diffraction, water attenuation, and reflection and transmission at the front and back surface of the sample. This chapter will open with background regarding these effects and then introduce the beam models. Since this research utilized the FSR, BSR1, BSR5 and BSR6 for estimation of the solid attenuation coefficient, their respective models will be presented. The rationale for using these specific reflections for attenuation coefficient estimation will be explained within the signal processing chapter.

The physics of a propagating acoustic wave is the catalyst for the diffraction field of a transducer. Furthermore, the specific diffraction field characteristics are dictated by the geometrical shape of the transducer's face (degree of concavity and radius) and the particular medium in which the emitted sound waves propagate. In order to better visualize the mechanics of a diffraction field, consider the face of a transducer to be comprised of an array of discrete points, where each point emits an acoustic wave front. As each wave front propagates into its medium, points of interference are created. These points of interference may be either constructive or destructive. Constructive interference amplifies the acoustic pressure, whereas destructive interference decreases the acoustic pressure. The specific location of local minima or maxima, referred to as nodes, within the diffraction field is controlled by the transducer geometry and the propagation medium. A focal node describes the point at which maximum acoustic pressure occurs and is said to be located at the transducer's focal length [7-10]. Since the location of each node depends upon the medium in which the sound waves propagate, the focal length for a given transducer will vary from one material to another. When propagation takes place in two materials, the focal node will still be representative of the point within the field having the highest acoustic pressure; however, the location of the focal node becomes dependent upon the two different medium's wave speeds. Consider a situation in which a sample having a thickness z_s and wave speed c_s is submersed within water having a wave speed c_w. An acoustic wave interrogates this sample at normal incidence, and it is desired to position the focal node at the back surface of the sample. In order to account for the wave speed variation across the two mediums, the total propagation distance is found as an equivalent water path distance, $2z_{we}$. The equivalent water path distance is equal to the actual water path distance plus the ratio of the water wave speed to sample wave speed, multiplied by the propagation distance within the sample. The equivalent water path distance for focusing on any *nth* back surface reflection, b_n , may be written as

$$2z_{webn} = 2z_{wbn} + \frac{c_s}{c_w} 2nz_s \tag{2.1}$$

With knowledge of the transducer's focal length in a purely water medium, Eq. (2.1) allows one to find the water path lengths which position the focal node at the desired back surface reflection, enabling equal diffraction measurements to be made across multiple reflections.

To illustrate the theoretical basis for equal diffraction points, an explicit derivation which yields equal diffraction points for two different water paths will now follow. Consider the acoustic pressure field of a focused transducer radiating into propagation mediums, *A* and *B*, with wave speeds, c_A and c_B, respectively. The propagation distance needed for focusing, with propagation in medium *A* only, is denoted x_A; and the distance for focusing, with propagation in medium *B* only, is x_B. If, for example, the wave speed c_B is twice the speed of c_A, $x_A$will be twice the distance of x_B. Since a paraxial condition is assumed at the interface between *A* and *B*, a change in wave speed is solely responsible for shifts in the position of the focal node; thus, the following constraint

$$x_A c_A = x_B c_B \tag{2.2}$$

can be placed on the diffraction effects between the two different mediums [10].

Tailoring this generic constraint towards the specific immersion mode testing used within this research, the water path distance for focusing on the front surface can be denoted z_{wf} , where the propagation speed within the water is c_w. In order for the diffraction effects at the back surface to be equivalent to the diffraction effects at the front surface, the following constraint must be satisfied

$$2c_w z_{wf} = 2c_w z_{wb1} + 2c_s z_s \tag{2.3}$$

where z_s is the sample thickness, c_s is the wave speed in the sample, and z_{wb1} is the water path required to achieve focusing on the back surface.

Dividing all terms within Eq. (2.3) by c_w, yields:

$$2z_{wf} = 2z_{wb1} + 2\frac{c_s}{c_w}z_s \tag{2.4}$$

It can be seen that this equation mirrors the form of Eq. (2.1), with z_{wf} substituted for the equivalent water path distance. After solving for z_{wb1}, the water path distance required for focusing to occur on the back surface is found to be

$$z_{wb1} = z_{wf} - \frac{c_s}{c_w}z_s \tag{2.5}$$

Applying the same methodology, the water path distance required for focusing at BSR5 and BSR6 can be written as

$$z_{wb5} = z_{wf} - 5\frac{c_s}{c_w}z_s \tag{2.6}$$

$$z_{wb6} = z_{wf} - 6\frac{c_s}{c_w}z_s \tag{2.7}$$

Equations (2.5 - 2.7) show that the water paths at the BSR1, BSR5, and BSR6 are dictated by the ratio of the wave speed in the sample to the wave speed in the water. Furthermore, the equal diffraction points for these locations are a function of the sample thickness. It may be seen that with knowledge of the wave speed in the sample, wave speed in the water, and sample thickness, the transducer may be positioned at an equal diffraction point for any desired back surface reflection.

2.2 Beam Models

As previously mentioned, the FSR, BSR1, BSR5, and BSR6 were used for estimation of the solid attenuation coefficient. Their respective models will now be introduced. All models are developed within the frequency domain assuming a linear, time invariant system. To denote the frequency dependent terms within the beam models, the nomenclature (f) will be used.

The FSR beam model is

$$F(f) = \beta_f(f) R_{ws} C\left(2z_{wf}, f\right) e^{-2z_{wf}\alpha_w(f)} \tag{2.8}$$

where β_f represents the system efficiency factor. This factor accounts for all transducer and electronic related effects on both the transmit side and the receive side. R_{ws} is the reflection coefficient which accounts for the portion of the acoustic wave that is reflected at the water to sample interface. $C\left(2z_{wf}, f\right)$ accounts for beam diffraction in the water, where $2z_{wf}$ is the round trip water path distance for the FSR; $e^{-2z_{wf}\alpha_w(f)}$ accounts for the water attenuation incurred by the acoustic wave as it propagates through the round trip water path distance; and α_w represents the water attenuation coefficient. It may be seen from the water attenuation term that more energy of the wave is diminished at longer water propagation distances. This same behavior occurs when the wave front propagates within the sample, as will be seen with the back surface reflection beam models. The BSR1 model follows from the form of the FSR model; however, there are additional terms which account for wave propagation within the sample. The BSR1 model may be written as

$$B_1(f) = \beta_{b1}(f) T_{ws} T_{sw} R_{sw} C(2z_{web1}, f) e^{-2z_{wb1}\alpha_w(f)} e^{-2z_s\alpha_s(f)} \tag{2.9}$$

T_{ws} and T_{sw} represent the transmission coefficient from the water to sample and sample to water, respectively, $e^{-2z_s\alpha_s(f)}$ accounts for attenuation within the sample, and α_s represents the solid attenuation coefficient. Since the transducer and electronic effects were not varied during the acquisition of all signals, β can be considered a constant; therefore, $\beta = \beta_f = \beta_{b1} = \beta_{b5} = \beta_{b6}$. Additionally, the term $T_{ws}T_{sw}$ may be reduced to $1 - R^2$. Adopting this new notation, the BSR5 and BSR6 models are respectively found to be

$$B_5(f) = \beta(f)(1 - R^2) R_{sw}^9 C(2z_{web5}, f) e^{-2z_{wb5}\alpha_w(f)} e^{-10z_s\alpha_s(f)} \tag{2.10}$$

$$B_6(f) = \beta(f)(1 - R^2) R_{sw}^{11} C(2z_{web6}, f) e^{-2z_{wb6}\alpha_w(f)} e^{-12z_s\alpha_s(f)} \tag{2.11}$$

2.3 EDC Nomenclature for Beam Models

The beam models formerly introduced provided conventional nomenclature for the water attenuation effects, diffraction effects, and reflection and transmission effects. To better distinguish implementation of the EDC approach for diffraction correction, nomenclature modifications for the beam models will now be presented. This change in nomenclature will also facilitate the explanation of the attenuation coefficient estimation process used within this work.

Since all signal processing steps were employed on magnitude spectra, a simplified notation will be adopted. Hereafter, the following substitutions will be made notation-wise (shown as applied to the FSR model terms)

$$F = |F(f)| \qquad \beta = |\beta(f)| \tag{2.12}$$

$$R = |R_{ws}| = |R_{sw}| \qquad C\left(2z_{wf}\right) = \left|C(2z_{wf}, f)\right|$$

This same type of nomenclature substitution will be made for the analogous terms within the back surface reflection models. To denote the application of the EDC approach within the beam models, the superscript * will be introduced. This nomenclature implies that the diffraction effects across all beam models are equivalent, that is, the diffraction terms are a constant; therefore, the constraint $C\left(2z_{wf}\right) = C(2z_{web1}) = C(2z_{web5}) = C(2z_{web6})$ must be satisfied. Consequently, this constraint requires that the propagation distance associated with each diffraction term maintain these equivalent diffraction effects; therefore, the constraint $z_{wf} = z_{web1} = z_{web5} = z_{web6}$ must also be satisfied. Selecting the diffraction field of the FSR as the reference for equivalent diffraction effects, the front surface water propagation distance z_{wf}^* inherently becomes the reference propagation distance. The water propagation distances required for equivalent diffraction effects at the FSR, BSR1, BSR5, and BSR6 follow from Eqs. (2.5 - 2.7) and may be written with the EDC nomenclature as

$$z_{wb1}^* = z_{wf}^* - \frac{c_s}{c_w} z_s \tag{2.13}$$

$$z_{wb5}^* = z_{wf}^* - 5\frac{c_s}{c_w} z_s \tag{2.14}$$

$$z_{wb6}^* = z_{wf}^* - 6\frac{c_s}{c_w} z_s \tag{2.15}$$

Having now introduced the EDC nomenclature, the diffraction terms of each back surface reflection will be shown as equivalent to the referenced FSR's diffraction term, $C(z_{wf}^*)$. Application of Eq. (2.1), with EDC nomenclature incorporated, renders the equivalent water propagation distances for the FSR, BSR1, BSR5, and BSR6 to be

$$2z_{web1}^* = 2z_{wb1}^* + \tfrac{c_s}{c_w} 2z_s \tag{2.16}$$

$$2z_{web5}^{*} = 2z_{wb5}^{*} + \frac{c_s}{c_w} 10z_s \tag{2.17}$$

$$2z_{web6}^{*} = 2z_{wb6}^{*} + \frac{c_s}{c_w} 12z_s \tag{2.18}$$

Through algebraic substitution, the diffraction terms across all back surface reflections may be shown as equivalent to the referenced FSR diffraction term as follows:

$$C(2z_{web1}^{*}) = C\left(2z_{wb1}^{*} + \frac{c_s}{c_w} 2z_s\right) = C\left[2\left(z_{wf}^{*} - \frac{c_s}{c_w} z_s\right) + \frac{c_s}{c_w} 2z_s\right] = C\left(2z_{wf}^{*}\right) \tag{2.19}$$

$$C(2z_{web5}^{*}) = C\left(2z_{wb5}^{*} + \frac{c_s}{c_w} 10z_s\right) = C\left[2\left(z_{wf}^{*} - 5\frac{c_s}{c_w} z_s\right) + \frac{c_s}{c_w} 10z_s\right] = C\left(2z_{wf}^{*}\right) \tag{2.20}$$

$$C(2z_{web6}^{*}) = C\left(2z_{wb6}^{*} + \frac{c_s}{c_w} 12z_s\right) = C\left[2\left(z_{wf}^{*} - 6\frac{c_s}{c_w} z_s\right) + \frac{c_s}{c_w} 12z_s\right] = C\left(2z_{wf}^{*}\right) \tag{2.21}$$

To better identify that the wave speed variation and sample thickness dictate the water path distance shift needed for focusing on each successive reflection, additional nomenclature will be introduced. Defining Δz_w^* as the water path distance shift, the following substitution can be made:

$$\Delta z_w^* = \frac{c_s}{c_w} z_s = z_{wf}^* - z_{wb1}^* = z_{wb5}^* - z_{wb6}^* \tag{2.22}$$

Integrating Δz_w^* into the water attenuation terms, the attenuation dependence on a changing water path is illustrated:

$$e^{-2z_{wb1}^*\alpha_w} = e^{-2\left(z_{wf}^* - \frac{c_s}{c_w}z_s\right)\alpha_w} = e^{-2z_{wf}^*\alpha_w} e^{2\frac{c_s}{c_w}z_s\alpha_w} = e^{-2z_{wf}^*\alpha_w} e^{2\Delta z_w^*\alpha_w} \tag{2.23}$$

$$e^{-2z_{wb5}^*\alpha_w} = e^{-2\left(z_{wf}^* - 5\frac{c_s}{c_w}z_s\right)\alpha_w} = e^{-2z_{wf}^*\alpha_w} e^{10\frac{c_s}{c_w}z_s\alpha_w} = e^{-2z_{wf}^*\alpha_w} e^{10\Delta z_w^*\alpha_w} \tag{2.24}$$

$$e^{-2z_{wb6}^*\alpha_w} = e^{-2\left(z_{wf}^* - 6\frac{c_s}{c_w}z_s\right)\alpha_w} = e^{-2z_{wf}^*\alpha_w} e^{12\frac{c_s}{c_w}z_s\alpha_w} = e^{-2z_{wf}^*\alpha_w} e^{12\Delta z_w^*\alpha_w} \tag{2.25}$$

Incorporating the newly introduced nomenclature for the EDC approach and water attenuation terms, the FSR, BSR1, BSR5, and BSR6 models may be written as follows:

$$F^* = \beta RC\left(2z_{wf}^*\right) e^{-2z_{wf}^*\alpha_w} \tag{2.26}$$

$$B_1^* = \beta(1-R^2)RC\left(2z_{wf}^*\right)e^{-2z_{wf}^*\alpha_w}e^{2\Delta z_w^*\alpha_w}e^{-2z_s\alpha_s} \tag{2.27}$$

$$B_5^* = \beta(1-R^2)R^9C\left(2z_{wf}^*\right)e^{-2z_{wf}^*\alpha_w}e^{10\Delta z_w^*\alpha_w}e^{-10z_s\alpha_s} \tag{2.28}$$

$$B_6^* = \beta(1-R^2)R^{11}C\left(2z_{wf}^*\right)e^{-2z_{wf}^*\alpha_w}e^{12\Delta z_w^*\alpha_w}e^{-12z_s\alpha_s} \tag{2.29}$$

2.4 Linearized Beam Models for Solid Attenuation Coefficient Estimation

Having written the beam models in such a way which emphasizes implementation of the EDC approach, the beam models will be transformed into an index notation form. This form will illustrate the functionality of the attenuation coefficient estimation method employed within this work. First, a solid attenuation term which explicitly shows zero propagation within the sample is incorporated into the FSR model. Additionally, F^* is now termed B_0^*.

$$B_0^* = \beta RC\left(2z_{wf}^*\right)e^{-2z_{wf}^*\alpha_w}e^{-0z_s\alpha_s} \tag{2.30}$$

Each model is then corrected for reflection, transmission, and changes in water attenuation as follows:

$$\bar{B}_0^* = \frac{B_0^*}{R} = \beta C\left(2z_{wf}^*\right)e^{-2z_{wf}^*\alpha_w}e^{-0z_s\alpha_s} \tag{2.31}$$

$$\bar{B}_1^* = \frac{B_1^*}{(1-R^2)Re^{-2\Delta z_w^* \alpha_w}} = \beta C\left(2z_{wf}^*\right)e^{-2z_{wf}^*\alpha_w}e^{-2z_s\alpha_s} \tag{2.32}$$

$$\bar{B}_5^* = \frac{B_5^*}{(1-R^2)R^9e^{-10\Delta z_w^* \alpha_w}} = \beta C\left(2z_{wf}^*\right)e^{-2z_{wf}^*\alpha_w}e^{-10z_s\alpha_s} \tag{2.33}$$

$$\bar{B}_6^* = \frac{B_6^*}{(1-R^2)R^{11}e^{-12\Delta z_w^* \alpha_w}} = \beta C\left(2z_{wf}^*\right)e^{-2z_{wf}^*\alpha_w}e^{-12z_s\alpha_s} \tag{2.34}$$

The term $\beta C(2z_{wf}^*)\ e^{-2z_{wf}^*\alpha_w}$ is shared between all reflections, effectively making it a constant with respect to z_s; therefore, the following substitution is made:

$$\Phi = \ \beta C\left(2z_{wf}^*\right)e^{-2z_{wf}^*\alpha_w} \tag{2.35}$$

Equations (2.31 – 2.34) may now be written as follows:

$$\bar{B}_0^* = \Phi e^{-0z_s\alpha_s} \tag{2.36}$$

$$\bar{B}_1^* = \Phi e^{-2z_s\alpha_s} \tag{2.37}$$

$$\bar{B}_5^* = \Phi e^{-10z_s\alpha_s} \tag{2.38}$$

$$\bar{B}_6^* = \Phi e^{-12z_s\alpha_s} \tag{2.39}$$

A general equation can be derived from Eqs. (2.36 – 2.39) as follows

$$\bar{B}_n^* = \Phi e^{-2nz_s\alpha_s} \tag{2.40}$$

Taking the natural logarithm of Eq. (2.40) leads to the linearized form:

$$\log(\bar{B}_n^*) = \log(\Phi) - 2nz_s\alpha_s \tag{2.41}$$

From this linearized form, it may be seen that a plot of $\log(\bar{B}_n^*)$ versus the propagation distance within the sample, that is, $2nz_s$, will render an estimate on the solid attenuation coefficient, with the slope being equivalent to $-\alpha_s$.

2.5 Frequency Dependence in Attenuation and Grain Size Correlation

The frequency dependence of attenuation and the attenuation coefficient's correlation with the sample's mean grain diameter will now be discussed. As a wave propagates within a medium, the attenuation increases with increasing frequency. Specifically, the attenuation coefficient is seen to be a function of frequency as follows:

$$\alpha = af^{b} \tag{2.42}$$

where a is a constant which is dependent upon the propagation medium's microstructural properties, f is the frequency of interest within the acoustic wave's frequency spectrum, and b is a constant whose value is dictated by the dominant scattering regime of the propagation medium. The currently accepted theory for the scattering of ultrasonic waves defines 3 separate scattering regimes, where each regime's threshold is controlled by the ratio of the wavelength to the mean grain diameter of the propagation medium. Although the scattering regime dominant within each sample was not of primary concern for the work done within this thesis, the criteria for each regime's threshold and expected energy loss are shown in Table 2.1. It should be noted that the right hand column shows $D\alpha$ rather than α, as suggested by [4, et al.].

Table 2.1. Scattering regimes' expected energy loss and range threshold.

Scattering Regime	Range Threshold	$D\alpha$
Rayleigh	$D/\lambda \ll 1$	$A_r \frac{D^4}{\lambda^4}$
Stochastic	$D/\lambda \approx 1$	$A_s \frac{D^2}{\lambda^2}$
Diffusion	$D/\lambda \gg 1$	A_d

Within the table, D represents the mean grain diameter and $\lambda = \frac{c}{f}$, where λ is the wavelength, c is the wave speed within the propagation medium, and f is the frequency of interest. A_r, A_s, and A_d represent the scattering coefficients of the Rayleigh, Stochastic, and Diffusion regimes, respectively. These coefficients' values are based upon the microstructural properties of the scattering medium.

Rather than being concerned with what scattering regime was dominant within each sample, emphasis was placed on establishing the correlation between the attenuation coefficient and the mean grain diameter. This took priority since the quality of correlation was the governing factor for the accuracy of the grain diameter estimates.

To illustrate the basis for correlation model development, a general form will be given for the expected energy loss of each regime:

$$D\alpha = A\left(\frac{D}{\lambda}\right)^{s} \tag{2.43}$$

where A represents any one of the three regime's scattering coefficients, and s is a coefficient whose value is dependent upon the given regime. Since this general form exhibits a power law relationship, it becomes beneficial to linearize the relationship by taking the base-10 logarithm of Eq. (2.43) to yield:

$$\log_{10}(D\alpha) = \log_{10}(A) + s\log_{10}\left(\frac{D}{\lambda}\right) \tag{2.44}$$

With this form, a linear regression can be developed as a function of mean grain diameter, given that λ is held constant. It can be seen that increasing mean grain diameter produces a greater energy loss. Furthermore, the slope of the linear function is influenced by the scattering regime's power law relationship, specifically, the scatterer diameter. The LOO algorithm used for developing predictive grain size models from this linear correlation will be described within Chapter 5.

CHAPTER 3

Experimental Setup and Procedures

3.1 Experimental Hardware and Software

Ultrasonic testing was done in a water immersion mode using pulse-echo methods with a piezoelectric focused transducer. The experimental hardware consisted of the following major components: a stainless steel immersion tank containing deionized, filtered water, a pulser-receiver unit, a scanning bridge holding the transducer, a motor controller, an oscilloscope, and a PC containing a 12 bit A/D card. The experimental setup may be seen below in Fig. 3.1.

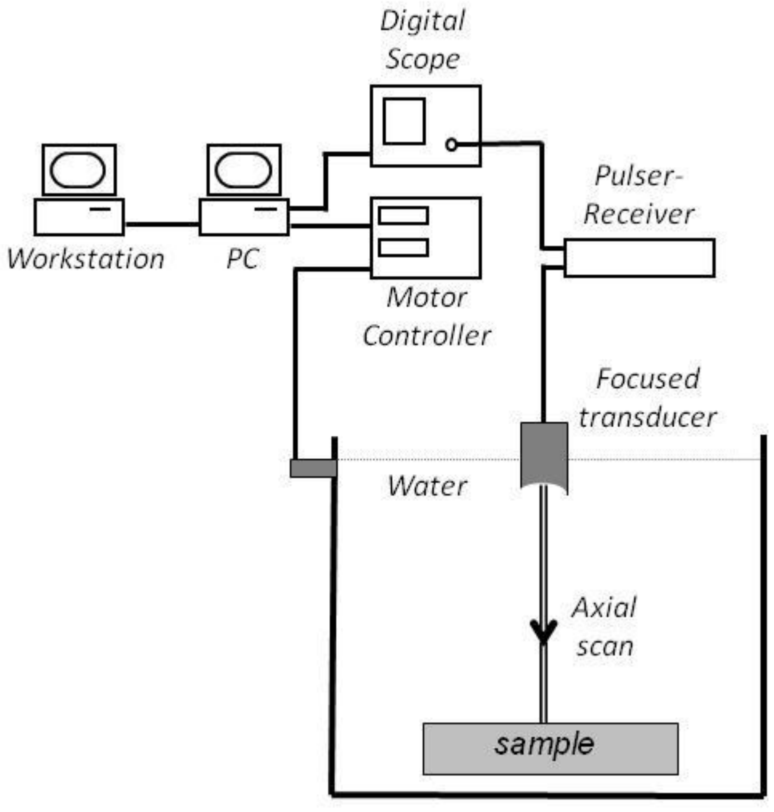

Fig. 3.1. Experimental set up [11].

Within the tank, two spacer blocks provided an interface between the sample and a leveling table. These blocks allowed the sample to be surrounded by the tank water on all exterior surfaces, ensuring that the absolute value of the reflection coefficients at the front and back surfaces of the sample would be equal. The use of the leveling table maintained normality between the central ray of the beam field and sample, regardless of the water path. The scanning bridge was positioned at the desired location through the use of 3 DC servo-motors. The motor controller executed the movement of the scanning bridge in the X, Y, and Z directions. The scanning bridge supported a search tube which held the transducer. A gimbal-swivel manipulator attached the transducer to the search tube. The manipulator contained two degrees of freedom for the angular position of the transducer, providing a means to normalize the transducer. The pre-scanning position of the transducer was manually controlled through the use of an input controller pad which directly interfaced with the motor controller. Scans were taken at an incrementally decreasing water path. The steps were controlled by the motor controller. The desired step values were set within a LabVIEW® software program [12] specifically tailored for axial scans (discussed in section 3.2). In addition to executing movement directions for the motor controller, the LabVIEW® program stored hardware/software settings (preamble information) pertinent to the specific scan. This information included the water temperature, pulser-receiver settings, and the axial scan parameters. The oscilloscope was connected to the pulser-receiver and was used for pre-scanning setup procedures (discussed in section 3.2). The pulser-receiver was capable of varying the electronic attenuation through manually controlled attenuation settings. These settings were meticulously adjusted for proper signal processing (discussed in section 3.2). For digitizing the analog scans, the PC utilized the high-speed 12-bit A/D card. The sampling rate for the card was 100 MHz, producing a large margin between the transducer frequency and the Nyquist Frequency of 50 MHz [9].

3.2 Pre-axial Scan Procedures and Axial Scans

An axial scan allows translation of the transducer in the Z direction (along the transducer's axis and perpendicular to the face of the sample) while the XY position is held stationary. At each new water path, an A-scan was acquired. Signal acquisition via axial scans enabled the EDC approach to be implemented through diffraction curve analysis (discussed in the signal processing chapter). Furthermore, axial scans allowed for an automated data acquisition process, as compared to manually positioning the transducer at each reflection's equal diffraction point; thus, the amount of overhead for experimental set up was greatly reduced.

Prior to monitoring any transmitted signals for pre-axial scan procedures, the transducer was lowered into the water and the lens' concavity was cleared of any trapped air bubbles. Since the presence of air at the face of the transducer creates an extremely high change in acoustic impedance, this simple step ensured that the full RF signal was transmitted from the face of the transducer into the water medium. Following this step, two pre-scanning normalization procedures were employed to ensure validity of the data taken. First, the sample was leveled so that the sound waves met the sample's surface at normal incidence, regardless of the water path distance. Precision leveling was carried out through an iterative process. This was done by scanning across the sample in the X and Y directions. As the transducer moved across an unleveled sample, the FSR translated in time. This time shift occurred due to the water path not being constant across all points of the sample; therefore, this provided an indication that one side of the sample was higher than the other. In order to correct for a non-uniform water path distance, a reference datum plane was chosen. This was done by placing a reference cursor on the oscilloscope at a water path time corresponding to the reference datum plane. To monitor the variability of the water path as a function of the sample's surface, the transducer was repeatedly passed across the face of the sample. During each pass, deviations in position of the FSR relative to the oscilloscope reference were monitored. At the close of each pass, the leveling plate was either raised or lowered to translate the FSR back to the reference time position. This methodical procedure was iterated until the FSR's position in time was nominally constant. Once the sample had been leveled in either the X or Y direction, the leveling process was employed in the same manner for the orthogonal direction.

The second normalization procedure involved the normalization of the transducer relative to the front surface of the sample. As was previously mentioned, a gimbal-swivel manipulator secured the transducer to the search tube (which is attached to the scanning bridge). The manipulator held two degrees of freedom for the transducer's angular position. The two arcs in which each angular position could be varied were orthogonal to one another. The angular position resulting in normal incidence was located by maximizing, or "peaking up", the FSR's amplitude. The amplitude was first peaked up while only varying the transducer's angular position within one arc. The angular position for normal incidence was located by monitoring the oscilloscope and identifying the point at which the FSR's amplitude was seen to increase and then abruptly decrease. Once the amplitude was peaked up for the first angular degree of freedom, the process was repeated in the same manner for the other orthogonal direction. This process was iteratively employed until the absolute maximum amplitude for the FSR was found.

Once normality had been verified, the transducer was moved axially through the entire water path range to search for waveform saturation at the waveform’s maximum amplitude. Identifying and eliminating saturation within the signal was essential for accurate waveform representation. Signal amplitude was maximized without saturation by optimizing the pulser–receiver attenuation setting. The optimum attenuation setting produced the largest amplified interface reflection without causing saturation. Identification of the waveform’s maximum amplitude was needed for determining the optimum digitization setting within the software. The optimum setting used the minimum digitization limit which was still capable of capturing the maximum amplitude. This produced the highest resolution for the targeted interface reflection by utilizing the majority of the 12 bits within the A/D card [10].

After correcting for saturation, the LabVIEW® software was used to target a specific time interval within the signal. Since attenuation coefficient estimates used the FSR, BSR1, BSR5, and BSR6, the time interval’s range was set to capture the wave train comprising these reflections. Due to an axial scan having an incrementally-decreasing water path, the LabVIEW® software was programmed so that the digitization window would follow the area of interest (the chosen time interval) as the water path continued to change. The time step value used to advance the time interval was determined through knowledge of the specified Z axis step value input to the software and the calculated wave speed in water. It should be noted that the actual time step value used was slightly extended relative to the calculated value. The lengthened time interval compensated for minute differences between the true water wave speed and calculated water wave speed, along with slight deviations in the motor controller's actual step increment. This ensured that the wave train of interest was fully digitized, despite the digitization window shifting in time at a slightly different rate than the wave train. A digitized A-scan containing an entire wave train may be seen below.

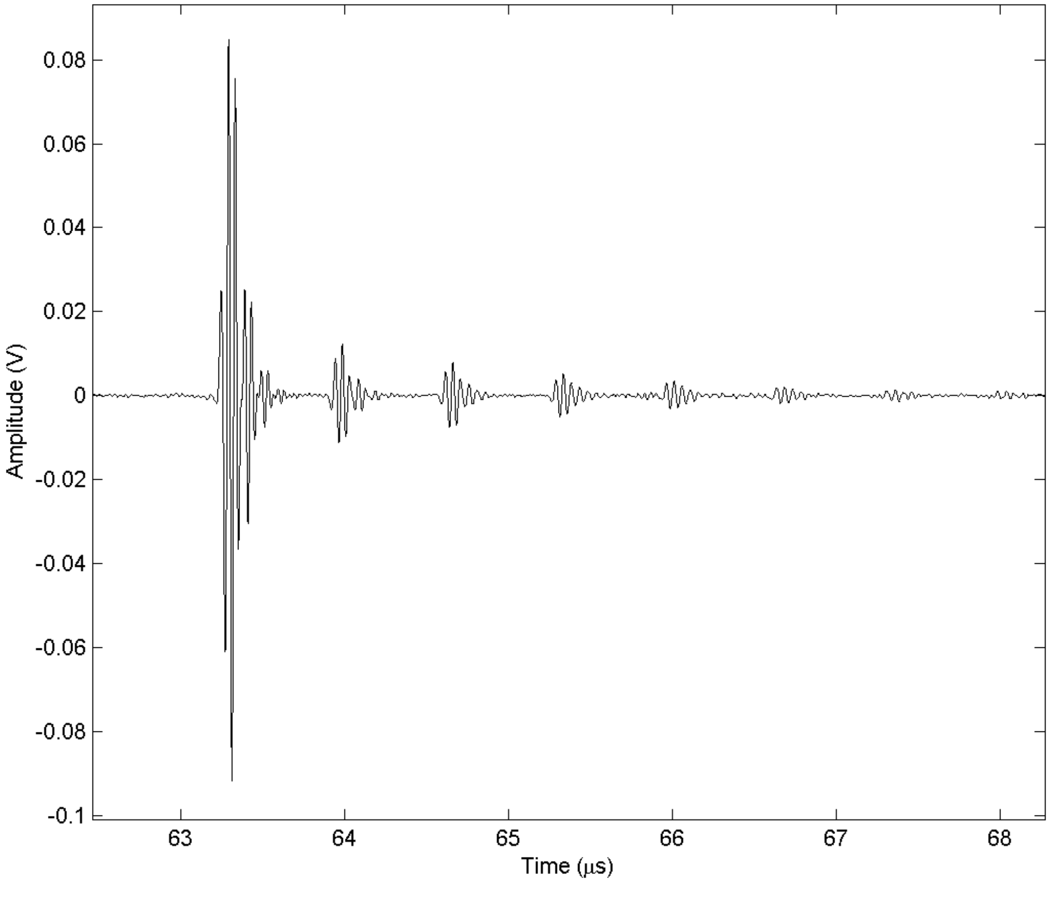

Fig. 3.2. Digitized A-scan comprising wave train of interest.

To more accurately calculate the wave speed in the water, a temperature measurement was taken with a digital-readout thermocouple just prior to running an axial scan. The obtained temperature was entered into the LabVIEW® software, and the wave speed in the water was calculated per the literature [13]. Additionally, the water temperature was needed for determining the water attenuation coefficient, as calculated per the literature [14]. The transducer was initially positioned at a long water path and then incremented at steps of 1 mm towards the sample. The initial and final water paths of the transducer were selected at positions which ensured that all reflections' diffraction curves were fully developed. Specifically, the initial water path was chosen at a location which was prior to the peak of the FSR's diffraction curve, and the final water path was located at a position following the BSR6's diffraction curve peak. Full development was essential for the diffraction curves to be properly smoothed with a polynomial during diffraction curve analysis, as will be discussed in the signal processing chapter. Once the initial and final water path distances were established, the translation distance of the transducer and Z axis step increment were used to calculate the number of Z axis steps required. This parameter was then input into the LabVIEW® software. Finally, at each axial scan position, the wave train within the time interval was digitized and written into a file, along with preamble information, for subsequent transfer to a data analysis computer for signal processing.

3.3 Sample Wave Speed Estimation

Measurements were made on each sample using a planar transducer. This data was used to estimate the time-of-flight in the sample, Δt_s. Sample placement, leveling, and normalization procedures were the same as described above; however, only a single A-scan for each sample was needed, thus axial scans were not used.

The time-of-flight values were used in conjunction with each sample's measured thickness to obtain the sample wave speed. Thickness measurements were taken at 5 different locations across the sample using a digital micrometer. The mean thickness of these measurements was used for calculation of the sample's wave speed.

CHAPTER 4

Signal Processing and Analysis

This chapter opens with a brief description of the approach used for wave speed estimation. The remainder of the chapter describes the signal processing and analysis employed for estimating the attenuation coefficients from axial scan data and the correlation of attenuation coefficient estimates with mean grain diameter.

4.1 Time-of-Flight in the Sample

The signal processing utilized for estimation of each sample's wave speed was employed on data acquired separately from the axial scan data. Each sample's data set consisted of a single A-scan containing the FSR and BSR1. The time-of-flight in each sample, Δt_s, was estimated from planar transducer measurements, with a central frequency of 15 MHz. Time gates for the FSR and BSR1 were established, and the times associated with the absolute peak values of the FSR and BSR1, t_{sf} and t_{sb1}, were determined using the proprietary MATLAB® function max.m; Δt_s was calculated as $t_{sb1} - t_{sf}$. Figure 4.1 shows a typical rectified A-scan with peak positions for the FSR and BSR1 identified.

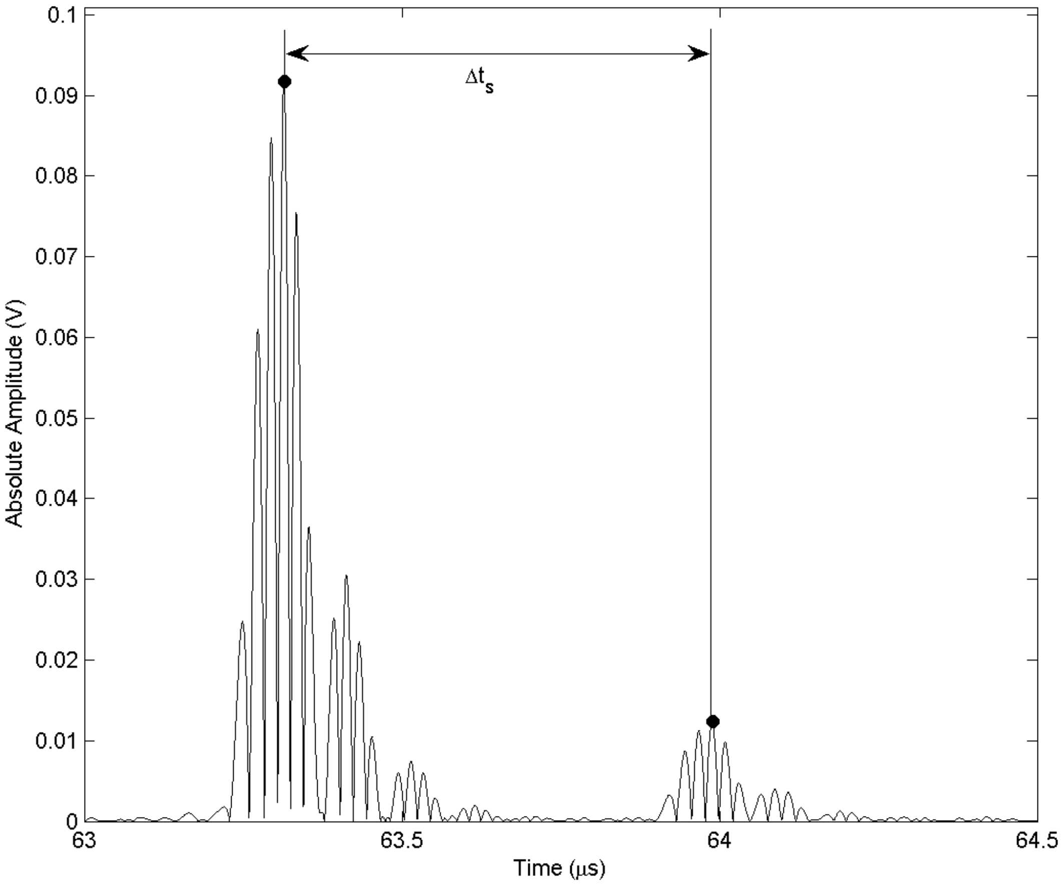

Fig. 4.1. A typical rectified A-scan showing the estimated time-of-flight for the sample.

4.2 Array Structuring for Axial Scan Data

After the completion of an axial scan, the digitized signals and corresponding preamble information were transferred as a binary data file to a networked data analysis computer. Multiple MATLAB® m-files [15], which were developed specifically for evaluating axial scans, were employed for signal processing. The algorithms used for interface reflection isolation and analysis required for attenuation coefficient estimation are explicitly discussed within this chapter.

In order to analyze the axial scan data, the signals were first retrieved from the binary data file and stored within a 2D MATLAB® array. The array was structured in such a way that each row corresponded to an A-scan acquired at a specific water path, where each element within a row represented a discrete voltage value. By knowing the sampling rate, the time interval between each digitized point was also known; therefore, a time vector corresponding to the voltage values was established. Figure 4.2 shows an image of the 2D array. The misalignment seen in the A-scans is addressed in section 4.2. Once the axial scan data was structured within the array, preliminary processing ensued.

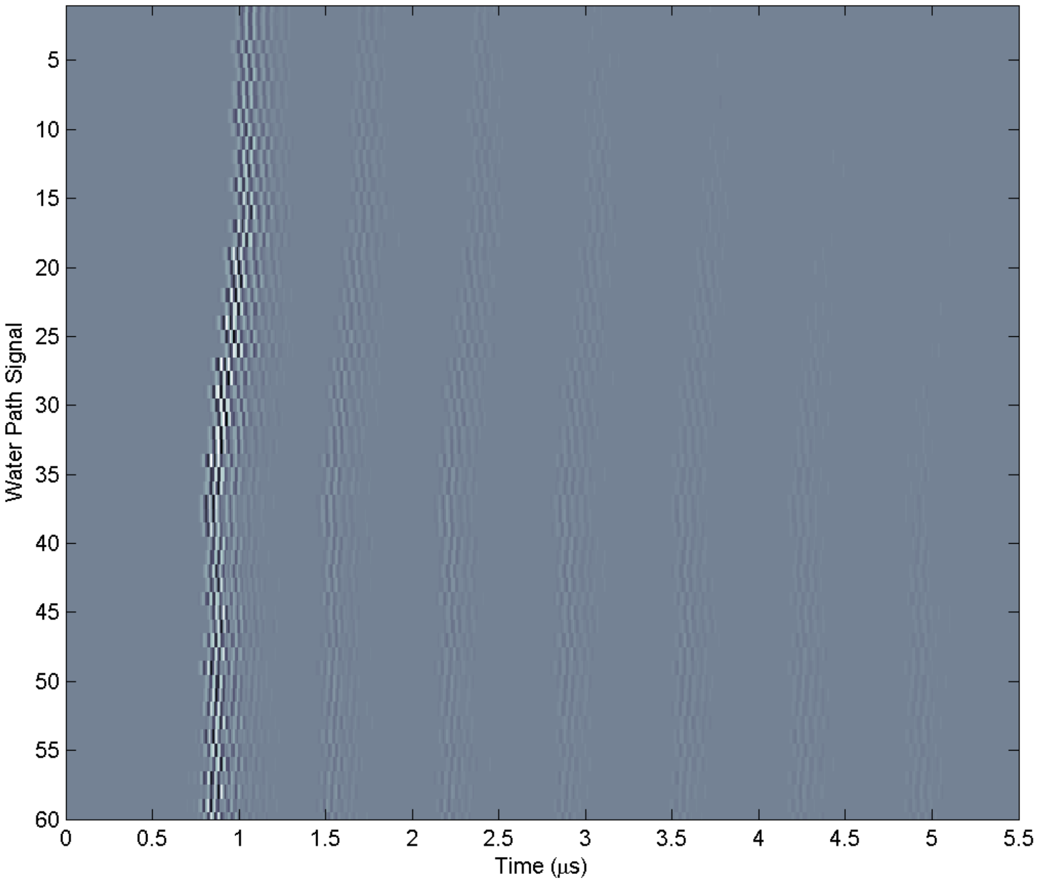

Fig. 4.2. Misaligned 2D array of A-scan signals.

Inherent within all data acquisition systems, resolution is limited in time by the digitization rate and in voltage by the number of bits available [10]. In an effort to decrease digitization effects, each A-scan was interpolated by means of a sinusoidal Fourier transform algorithm using the proprietary MATLAB® function interpft.m, effectively increasing the signal's resolution in the time domain. Figure 4.3 shows a digitized FSR before and after signal interpolation.

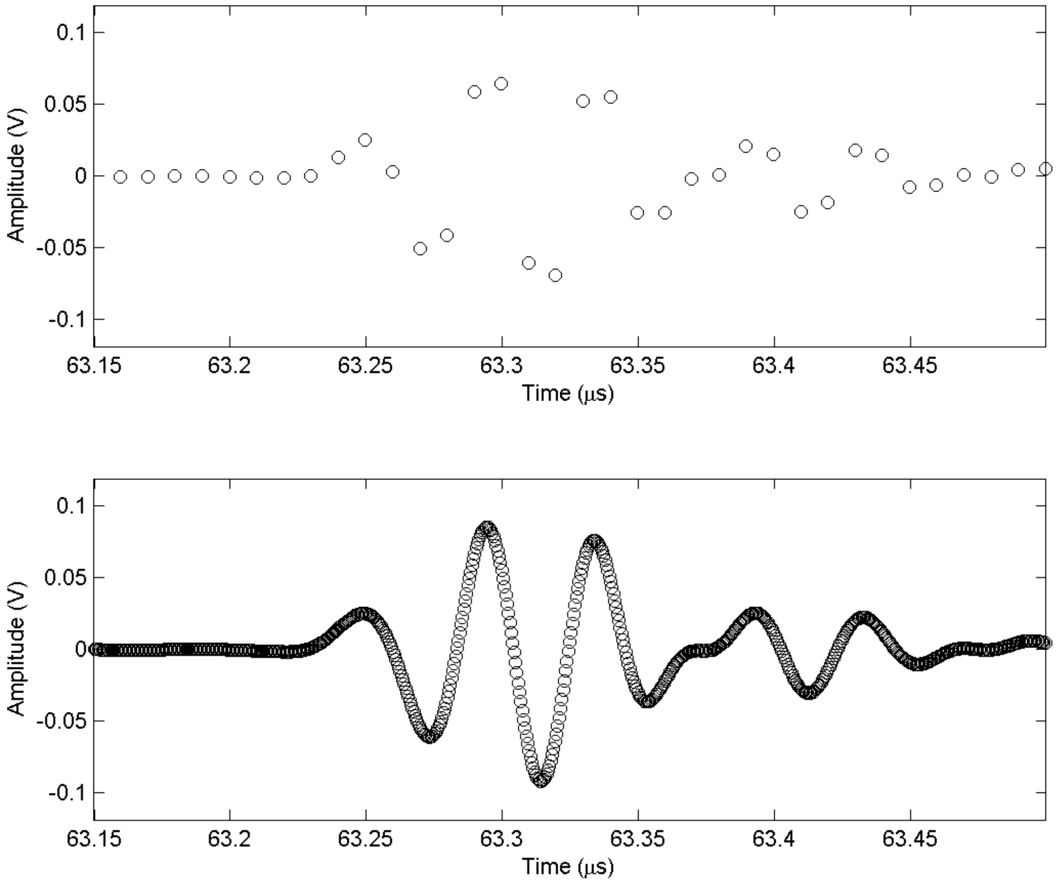

Fig. 4.3. Digitized FSR before and after signal interpolation.

4.3 Signal Alignment

Due to differences between the true water wave speed and calculated water wave speed, along with slight variability in transducer movement from step to step, each water path signal's FSR was located at a different time position. These non-uniform time positions created the misaligned array of signals seen in Fig. 4.2. To correct for the variation in the initial time of each FSR, each signal was aligned with a reference signal through a signal alignment algorithm. Implementation of this algorithm ensured that a user-defined time gate would completely envelope the interface reflection of interest so that its diffraction curve would be fully represented (discussed in section 4.5). The alignment algorithm utilized a trigger approach which detected a break in a user-specified voltage limit. The input voltage limit was set at a value which ensured that trigger detection would not mistake electronic noise for the onset of the FSR. The first absolute voltage value within each water path signal that exceeded the set voltage limit was used to determine the time position for signal alignment. This trigger element position was considered to be the onset of the FSR; however, due to each voltage value being discretized, the trigger's relative position within each FSR varied. As was previously mentioned, interpolation of the signals increased the resolution in time. Consequently, this reduced the variability in trigger time position for each different water path and increased the accuracy of the computed water attenuation filter, as will be explained below. Figure 4.4 shows the absolute amplitude of an FSR with identification of the trigger element position, that is, the onset of the FSR.

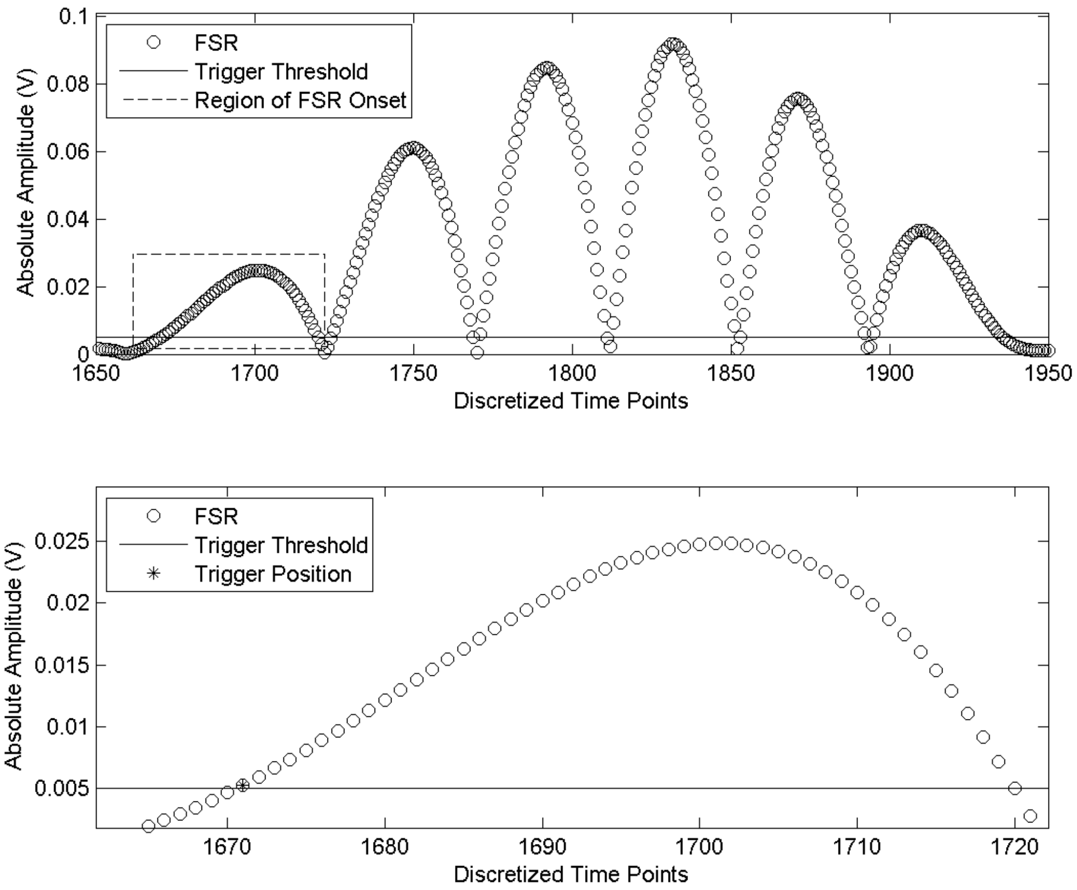

Fig. 4.4. Upper subplot shows rectified FSR with region of FSR onset identified, along with trigger threshold value. Lower subplot shows the determined trigger location.

After the trigger element position had been determined for every water path signal, each signal was shifted with respect to a reference trigger, where the reference trigger was the trigger element position for the mean trigger time. The trigger times, along with knowledge of the beginning time for the digitization window for each axial scan position, was used to calculate the water path time for each axial position, that is, for each A-scan as written into the rows of the 2D array. The beginning time for each digitization window was calculated based on user-specified inputs to the LabVIEW® program, which were stored in the preamble. Figure 4.5 shows an image of the aligned A-scans. The vertical axis gives the water path time for each axial scan position.

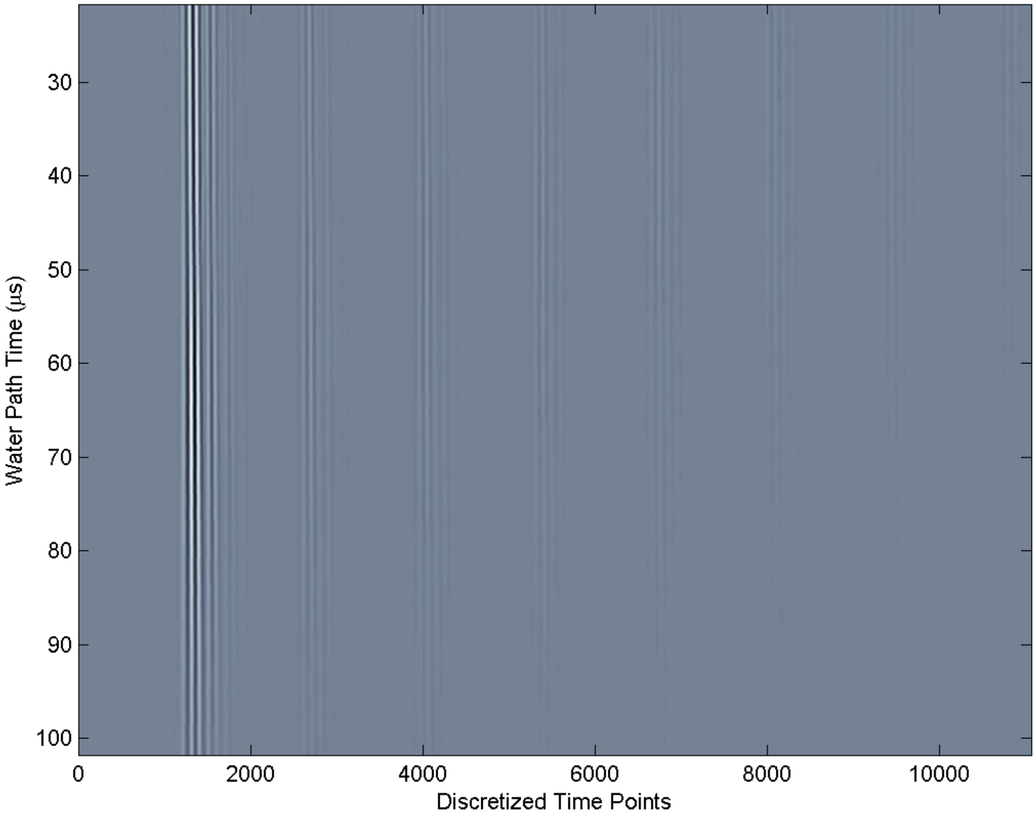

Fig. 4.5. Aligned 2D array of A-scan signals.

4.4 Interface Reflection Isolation and Correction of Water Attenuation and Reflection and Transmission Effects

Having knowledge of each water path time and the wave speed in the water, the water path distance corresponding to each acquired A-scan could be calculated. These calculated water path distances were needed to compute the water attenuation filter; therefore, the reduced variability in trigger position, relative to the FSR, resulted in a more accurate water attenuation filter. Recall from Chapter 2 that the amount of attenuation incurred within the water is represented by the term $e^{-2z_w\alpha_w(f)}$, where $2z_w$ represents the round trip water path distance and $\alpha_w(f)$ represents the frequency-dependent water attenuation coefficient. For the water attenuation filter to be computed, the water attenuation coefficient must be a priori knowledge. The water attenuation coefficient was calculated per the literature [14], and was dependent upon the measured water temperature and frequency range of interest. Before the water attenuation coefficient and filter were computed though, each reflection of interest was isolated with a user-specified time gate. Due to signal alignment, the time gate was able to encompass each reflection of interest for all water paths. Figure 4.6 shows the aligned 2D array of A-scans with time gates superimposed, enveloping each interface reflection of interest.

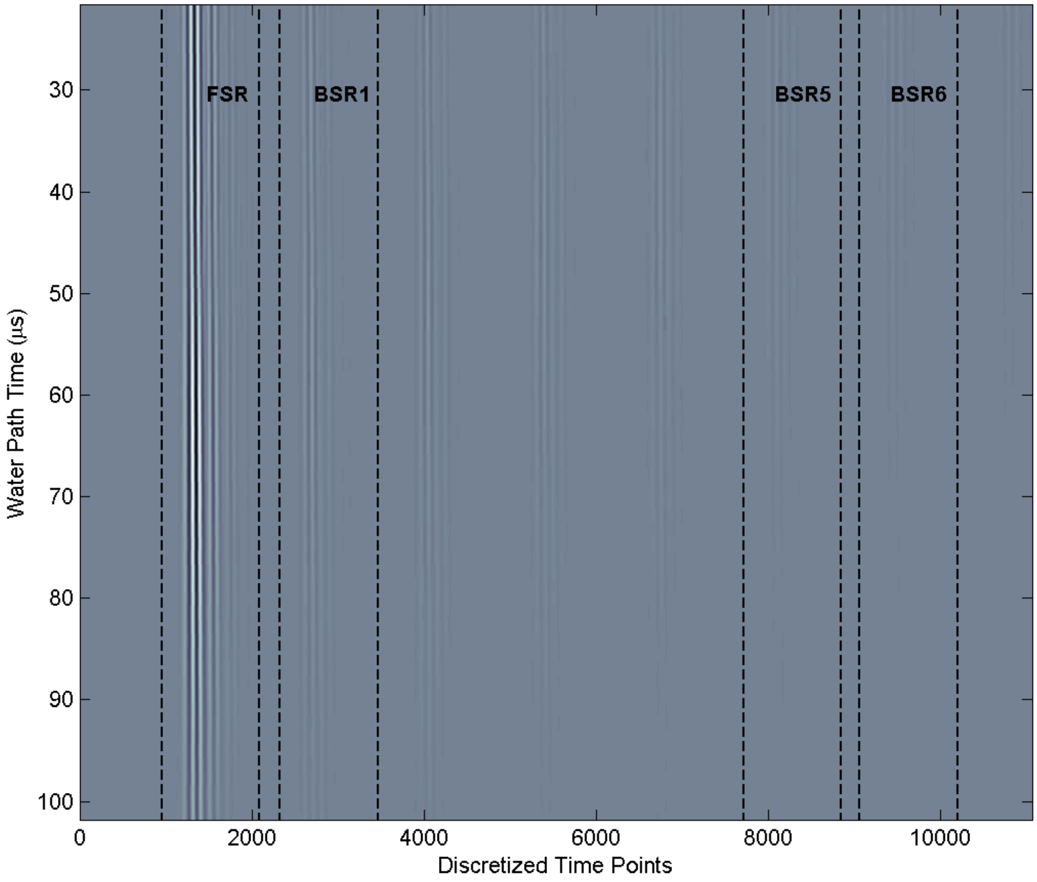

Fig. 4.6. Aligned 2D array of A-scan signals with time gates in place.

Within the time gate, the time element position of each reflection's peak absolute amplitude at each water path was determined using max.m. A Gaussian time window, normalized to unity, was then applied to each reflection within the time gate. The time element position corresponding to each reflection's peak value was used as the location for the mean of the Gaussian, that is, the position of the Gaussian's peak value. The Gaussian's standard deviation was set at a value that ensured approximately 95% of the Gaussian's area over laid the reflection of interest, with the tail ends over laying the remainder of the signal. The tail ends of the Gaussian eliminated all other reflections of the signal by effectively forcing them to zero. Figure 4.7 illustrates the application of a Gaussian time window to a typical FSR. The upper subplot consists of the FSR with its absolute peak value identified, the central subplot shows the Gaussian time window located at the peak value's time element position, and the lower subplot shows the FSR with the Gaussian time window applied.

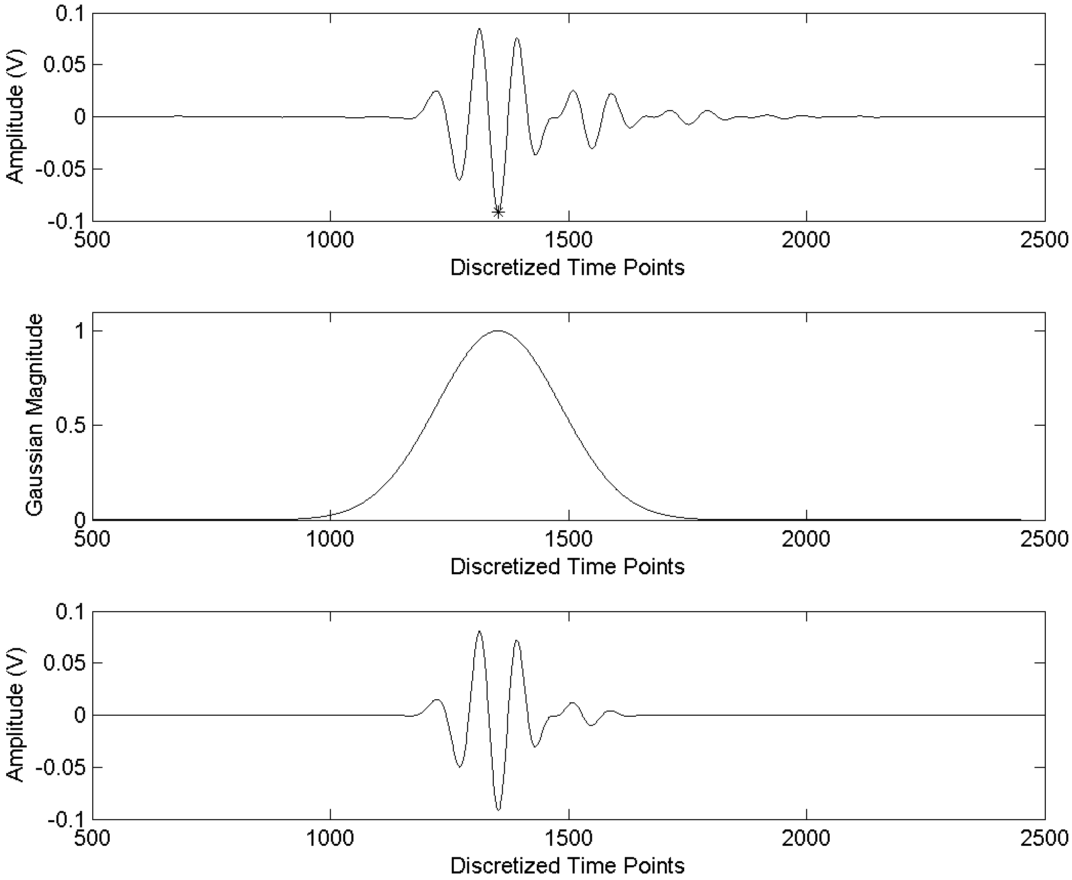

Fig. 4.7. Application of a Gaussian time window to an FSR.

Once each reflection had been isolated by means of the Gaussian time window, the Fast Fourier Transform (FFT) was taken. It should be noted that in order to maintain uniform discretized frequency values for all samples' data sets, the signals for each different axial scan contained the same number of discretized points in time. The FFT was applied to each isolated reflection using the proprietary MATLAB® function fft.m. The FFT was then applied to the isolated reflection for all water path signals, and the resultant magnitude spectra were superimposed on a single plot. Figure 4.8 shows the magnitude spectrums corresponding to the water path signals of an FSR, with the frequency gates applied. A user-specified frequency range was selected for further processing. The selected range enveloped the central frequencies for all water paths.

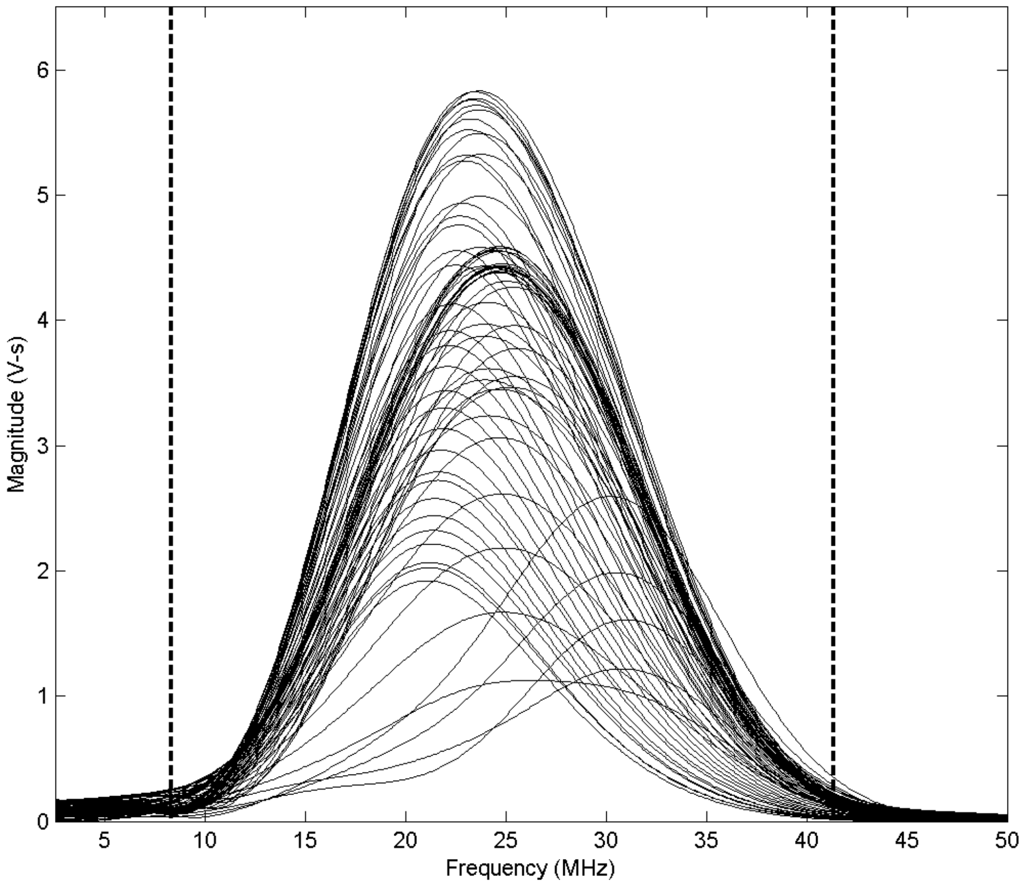

Fig. 4.8. Magnitude spectrums of an FSR at all water paths, with the frequency range selected for further processing identified by the dashed vertical lines.

The user-specified frequency range was then held constant for the remainder of the reflections, that is, the BSR1, BSR5, and BSR6. The reason for maintaining a constant frequency range will be explained in section 4.8. For the selected frequency range, an inverse water attenuation filter was computed and applied to each isolated reflection [16]. This inverse water attenuation filter effectively canceled the water attenuation expected at each water path distance for the frequencies of interest. This filter was of the form $e^{2z_{wf}\alpha_w(f)}$, where all coefficients represent the quantities previously defined within Chapter 2. Figure 4.9 shows a 3D contour of the calculated filter.

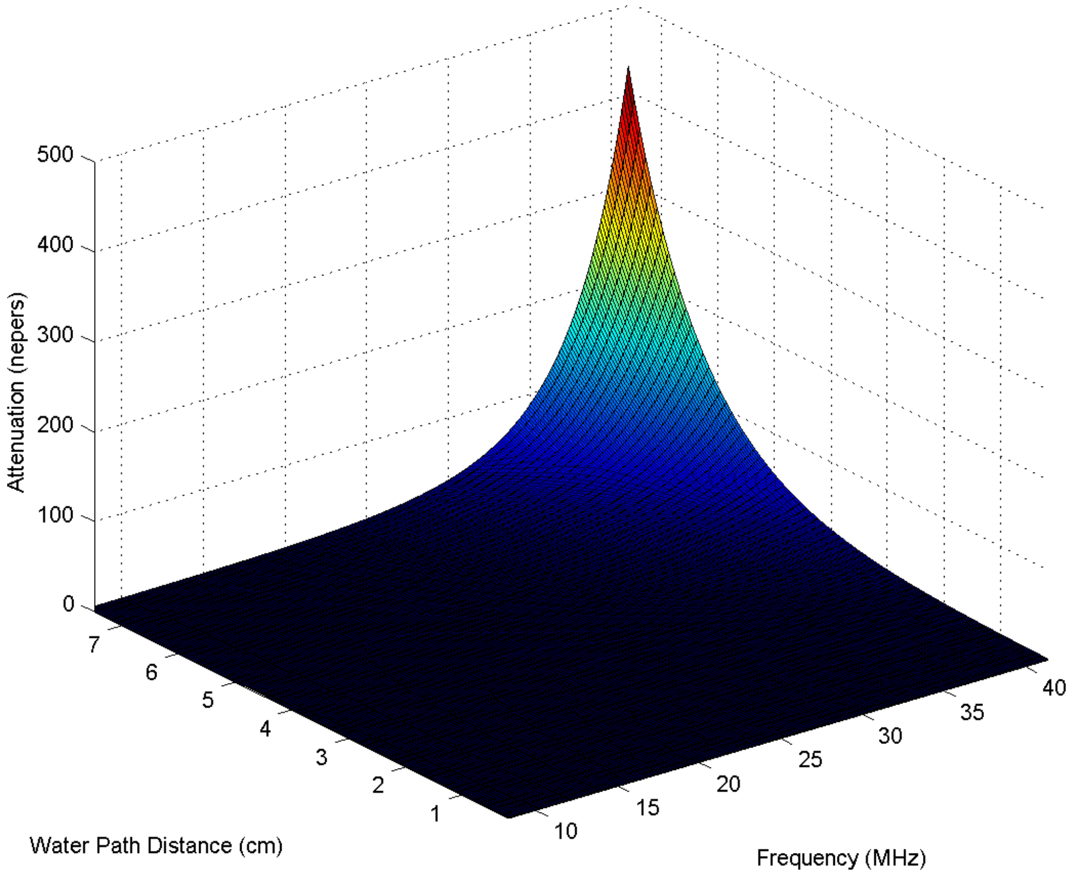

Fig. 4.9. Inverse water attenuation filter shown as a function of water path distance and frequency.

Finally, each magnitude spectrum, at each water path, was corrected for transmission and reflection effects as shown in Eqs. (2.31 – 2.34). An estimate on the reflection coefficient was obtained through knowledge of the sample's density and experimentally calculated wave speed, along with the calculated wave speed in water and known water density. The magnitude spectrums of each interface reflection were divided by their appropriate reflection and transmission coefficient terms.

4.5 Frequency Domain Diffraction Curve Development

After each reflection had been isolated and its magnitude spectrum had been corrected for water attenuation and transmission and reflection effects, frequency domain diffraction curves were developed.

Each diffraction curve corresponded to a discrete frequency within the selected frequency range. The reflection's equal diffraction point was taken at the location corresponding to the transducer's maximum focus. The maximum value in each diffraction curve, at each frequency, for each reflection, was taken as the corresponding value of $\bar{B}_n^*$, as given in Eqs. (2.36-2.39). The identification and selection of each diffraction curve's peak value was carried out utilizing a polynomial smoothing algorithm. This algorithm will be discussed in section 4.6. A typical diffraction curve corresponding to a discrete frequency of interest may be seen in Fig. 4.10.

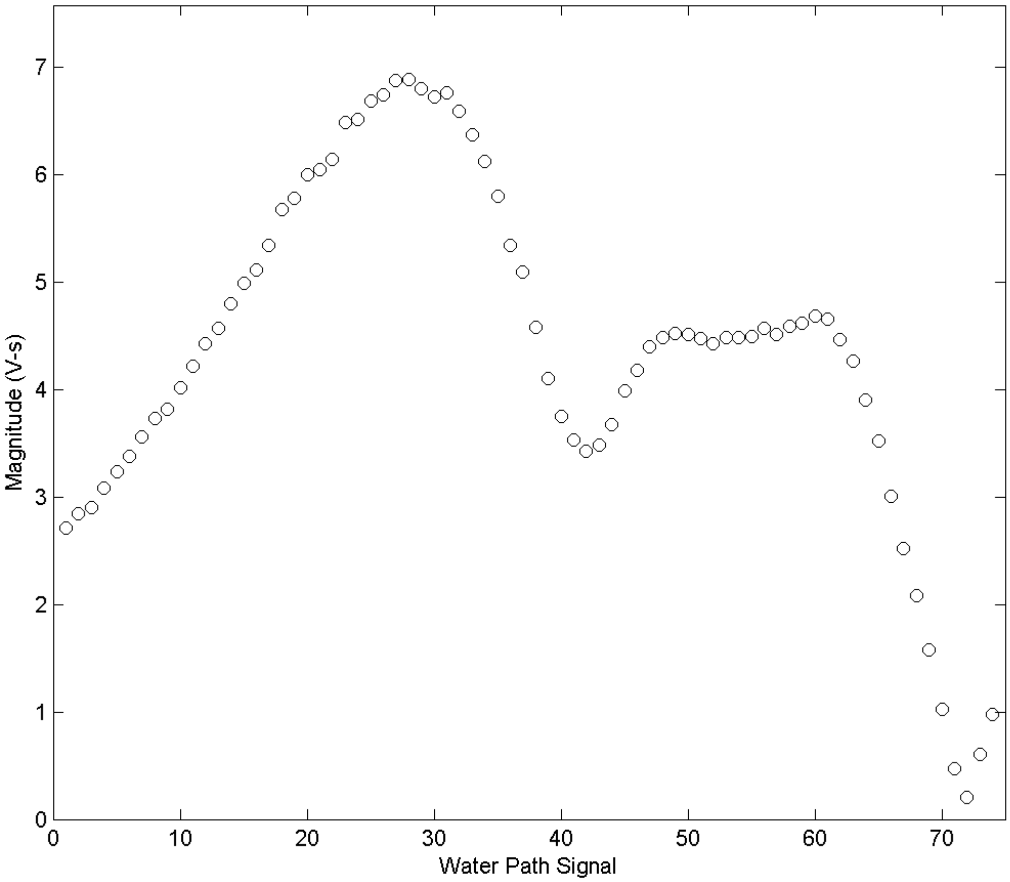

Fig. 4.10. Diffraction curve of a single frequency.

The diffraction curves were developed by monitoring each frequency's magnitude values across all water paths. To facilitate the explanation of the diffraction curve algorithm, consider an aligned 2D array consisting of 25 A-scans, that is, 25 different water paths. A reflection of interest has been isolated (Fig. 4.6 and 4.7) and converted to the frequency domain, and the selected frequency range (Fig. 4.8) is comprised of 10 discrete frequencies. From these given parameters, the isolated reflection would contain 10 diffraction curves, each corresponding to a different frequency. Additionally, each diffraction curve would contain 25 magnitude values, where each value corresponds to a different water path. By plotting the magnitude values as a function of water path, each frequency's degree of focus, as the transducer translates towards the sample, would be observed.

Applying the previous example to the axial scan data acquired in this research simply results in a greater number of frequencies monitored over a larger water path range. The diffraction curves for each frequency were plotted on a single figure, allowing the peak region of all diffraction curves to be identified. A user-specified water path gate was used to select the range over which each diffraction curve would be smoothed via the polynomial smoothing algorithm. Figure 4.11 shows the frequency domain diffraction curves corresponding to an isolated FSR, with water path gates superimposed. Due to a high number of discretized frequencies being monitored, the diffraction curves merge together, hindering the ability to differentiate individual diffraction curves; however, the peak region of the curves is still apparent.

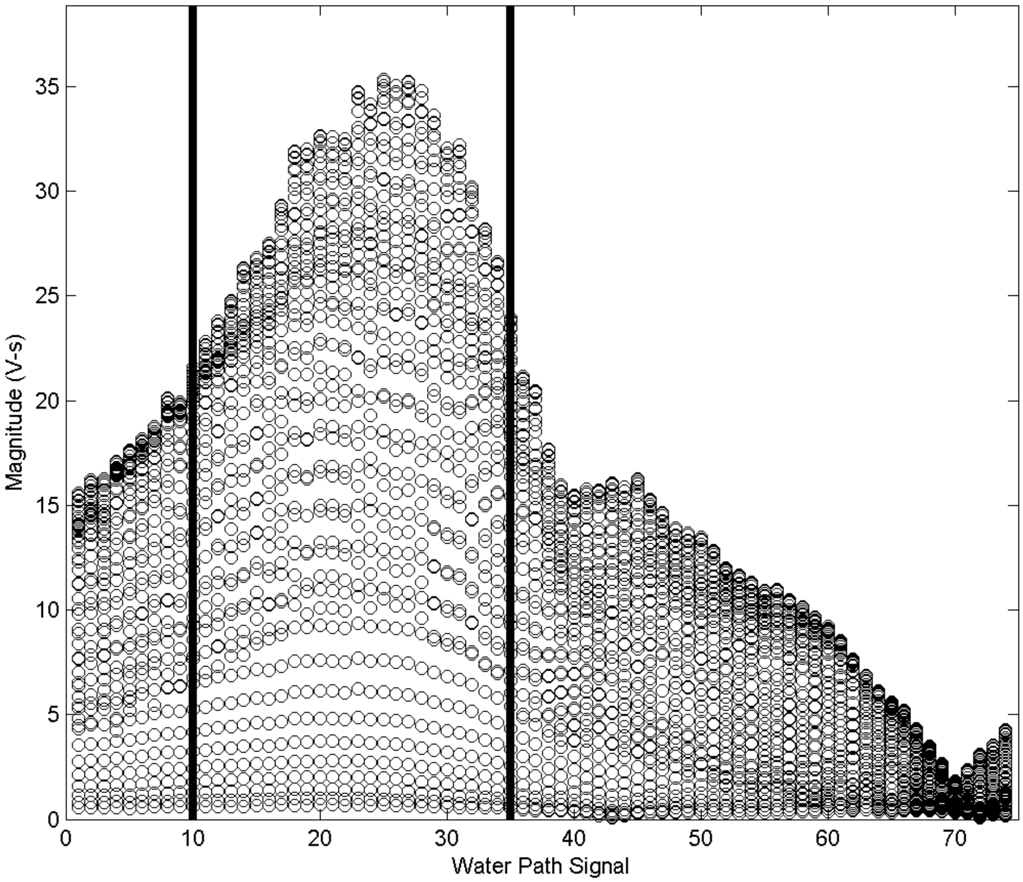

Fig. 4.11. Frequency domain diffraction curves of an isolated FSR with the water path range used for polynomial smoothing identified by the solid lines.

4.6 Polynomial Smoothing of Diffraction Curves

Once diffraction curves had been developed, a polynomial smoothing algorithm was implemented. Given the finite number of water paths, polynomial smoothing was utilized to more accurately determine each diffraction curve’s true peak magnitude. Polynomial smoothing was used for both smoothing of random variations in the diffraction curves and as a basis for polynomial interpolation to effectively increase the number of water path points.

The raw data diffraction curves were modeled using a polynomial curve-fitting algorithm, polyfit.m in MATLAB®. A water path range was selected for smoothing each diffraction curve. In addition to specifying the range for curve fitting, the degree of polynomial was specified (an 8th order polynomial was used within this research). Since the equal diffraction points were contingent upon the maximum or peak value, the water path range selected for curve fitting primarily included the upper portion of the diffraction curve. This ensured that the polynomial predominantly fitted the diffraction curve in the region of the peak. The polynomial was then evaluated at an increased density of data points, using the proprietary MATLAB® function polyval.m. The increased number of data points improved the likelihood of selecting a data point located at the defined polynomial's true maximum. The function max.m was implemented within the fitted diffraction curve range to determine its peak magnitude. The identified value was taken as the equal diffraction point for the given frequency, again $\bar{B}_n^*$, as given in Eqs. (2.36 - 2.39). This algorithm was implemented for each reflection over the selected frequency range, and each frequency's identified peak value was stored into an array. Figure 4.12 shows a 3D contour of each reflection's polynomial smoothed diffraction curves.

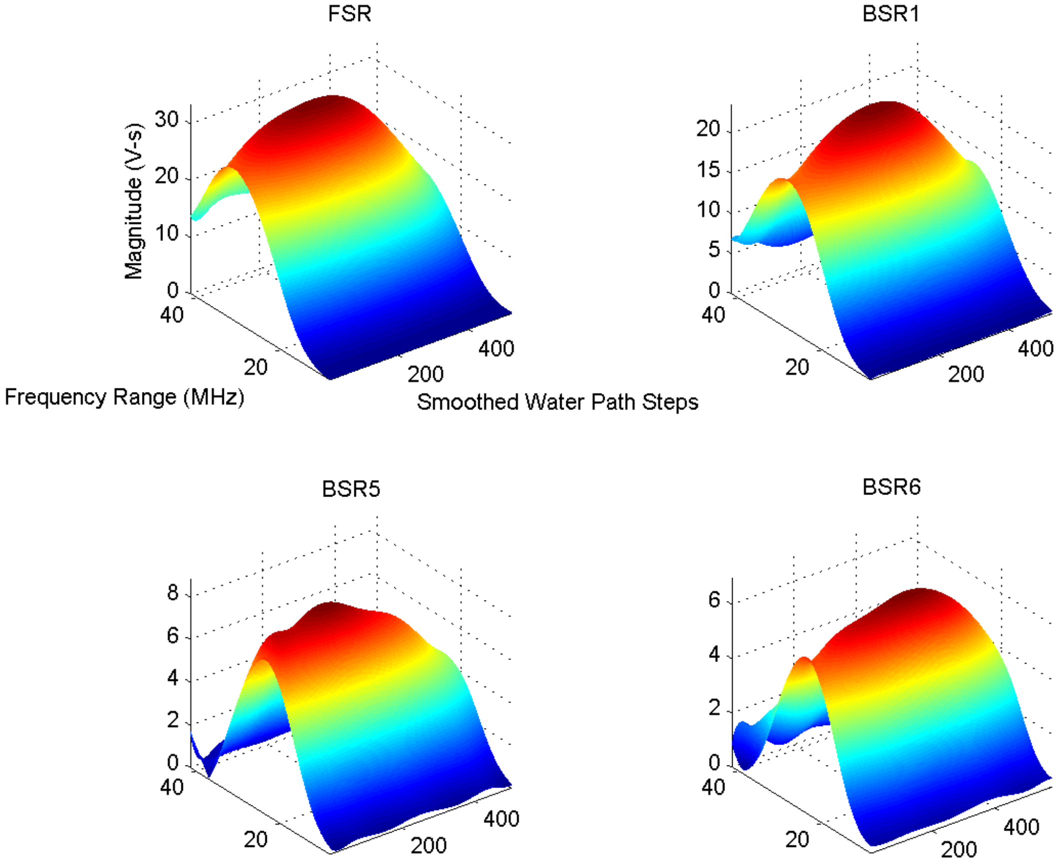

Fig. 4.12. Polynomial smoothed diffraction curves of the FSR, BSR1, BSR5, and BSR6.

4.7 Regression Fits for Solid Attenuation Coefficient Estimation

Once the equal diffraction points, $\bar{B}_n^*$, had been identified for all frequencies, estimation of the solid attenuation coefficient followed. For each discrete frequency, $\log(\bar{B}_n^*)$ was plotted versus the propagation distance within the sample, $2nz_s$, as represented in Eq. (2.41). As was derived in Chapter 2, the negative slope of a linear regression, fitted to this data, yielded an estimate on the solid attenuation coefficient. Since the FSR, BSR1, BSR5, and BSR6 were utilized for attenuation coefficient estimation, the solid propagation distance was relatively large, as would be compared to using back surface reflections grouped closer in time to the FSR. Given that all samples were relatively thin, the longer sample propagation distance provided better leverage in estimating the slope of the $\log(\bar{B}_n^*)$ versus $2nz_s$ line. A linear regression was applied using polyfit.m with the negative slope of the regression line yielding the attenuation coefficient estimate at each frequency, $\alpha_s(f)$. The solid attenuation coefficient estimate, for each frequency, was stored into an array. A typical linear regression applied at a single frequency may be seen in Fig. 4.13.

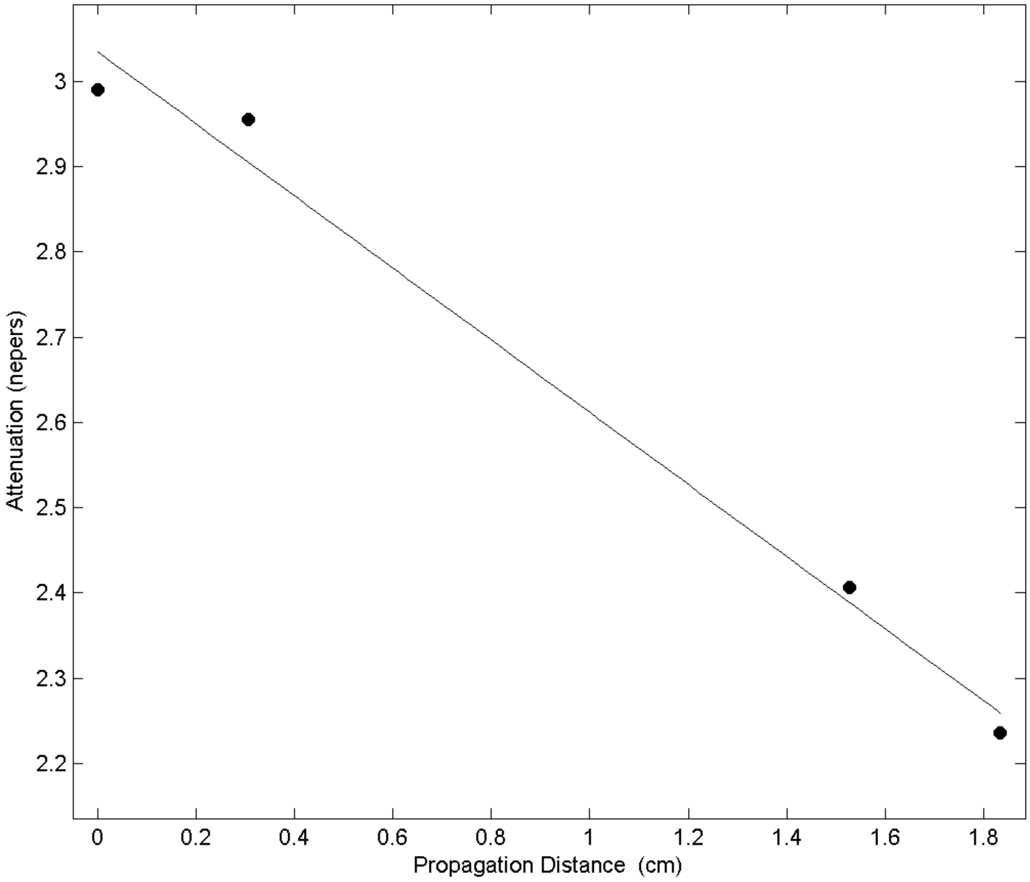

Fig. 4.13. Linear regression representing a negative-valued attenuation coefficient estimate at a single frequency.

All signal processing steps previously discussed within sections 4.2 - 4.7 were applied towards each sample’s axial scan data. After analysis of each sample, parameters of interest, namely the solid attenuation coefficient and frequency range, were stored within a MATLAB .mat file for further analysis.

4.8 Grain Diameter – Attenuation Correlation

After each sample’s attenuation coefficient had been estimated and stored, the .mat files were imported back into the active MATLAB® environment for further data analysis. An additional m-file, developed for correlation analysis, was implemented on the parameters saved within the .mat files. Before correlation plots could be generated, a frequency range shared between all samples needed to be specified. This was due to the frequency range corresponding to each sample’s attenuation coefficient estimates being slightly different. These differences were a result of the frequency range being graphically specified for each sample. Figure 4.14 shows the attenuation coefficient estimates plotted against frequency for all 5 samples. Since the attenuation coefficient estimates fell below zero at lower frequencies for certain samples, only the high-end frequency estimates were utilized in the correlation analysis. The region containing the frequency range used is identified with a hashed box in Fig. 4.14. Figure 4.15 provides a magnified view of the positive-valued region, along with the frequency gates utilized for ensuring a shared estimate range between the samples.

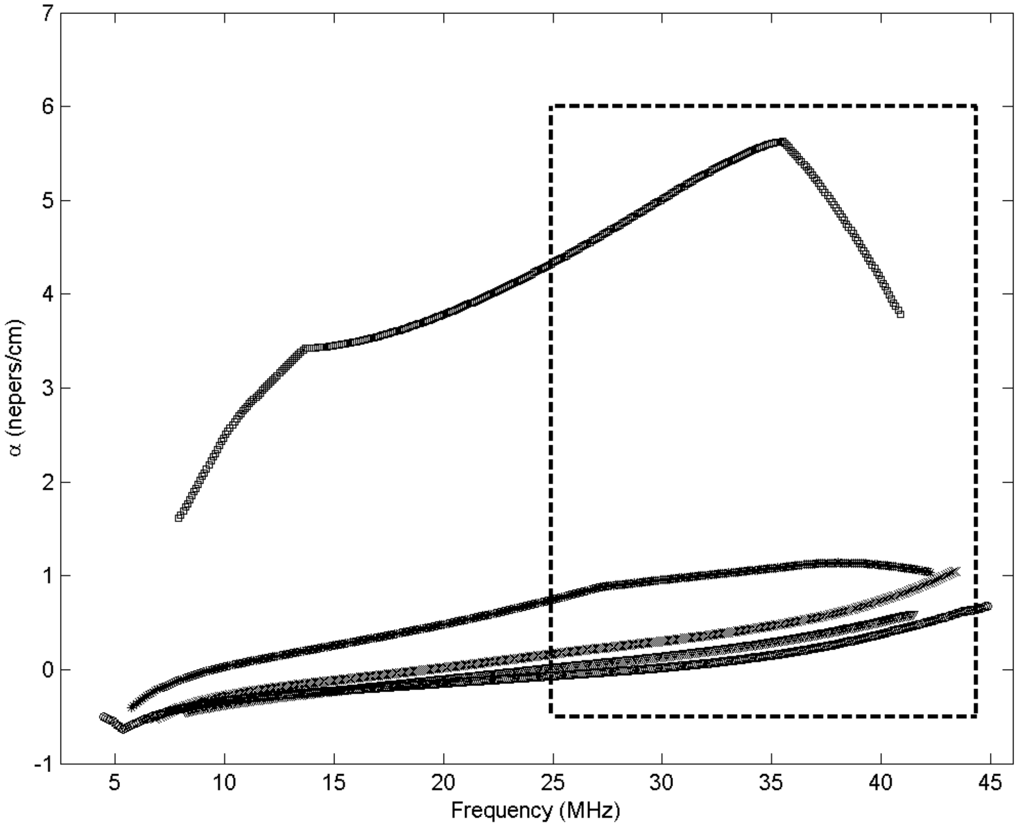

Fig. 4.14. Attenuation coefficient estimates versus frequency for all samples with the frequency region of interest identified.

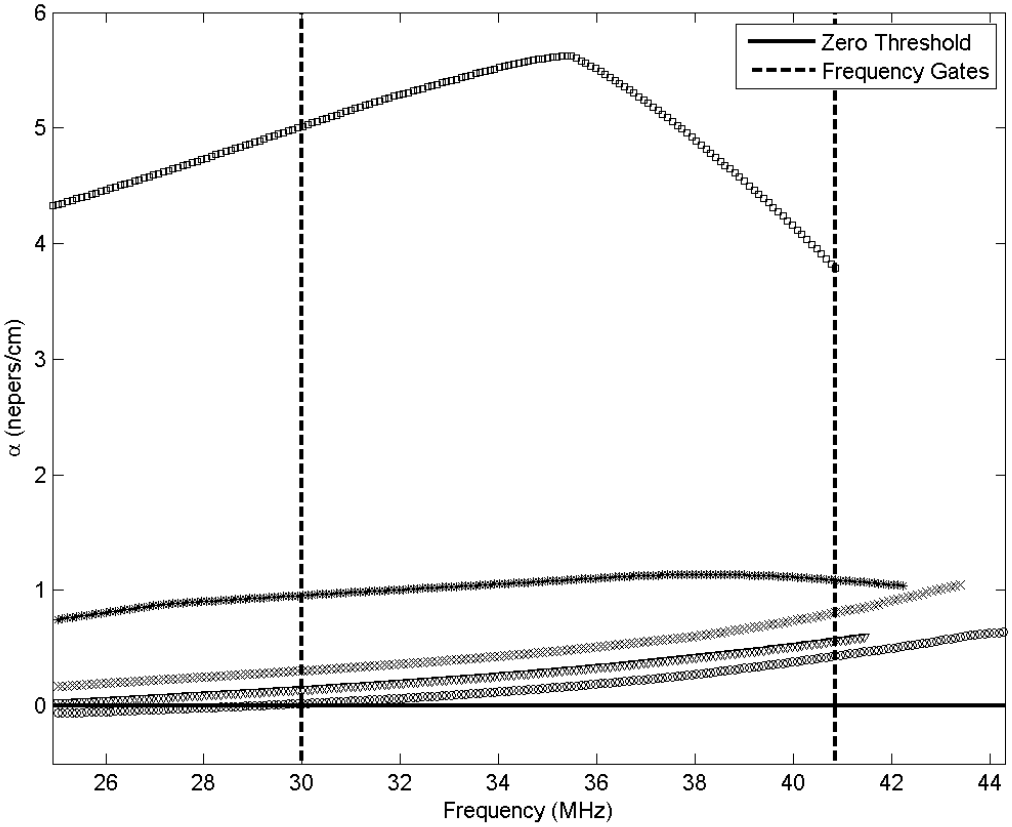

Fig. 4.15. Magnified view of positive-valued estimate region, with frequency gates superimposed.

At each discrete frequency within the specified frequency range, the attenuation coefficient estimates were plotted versus mean grain diameter, as shown in Fig. 4.16. Additionally, Fig. 4.17 shows these estimates as a function of mean grain diameter on a base-10 logarithmic scale. The strong correlation between solid attenuation and mean grain size is evident in both figures.

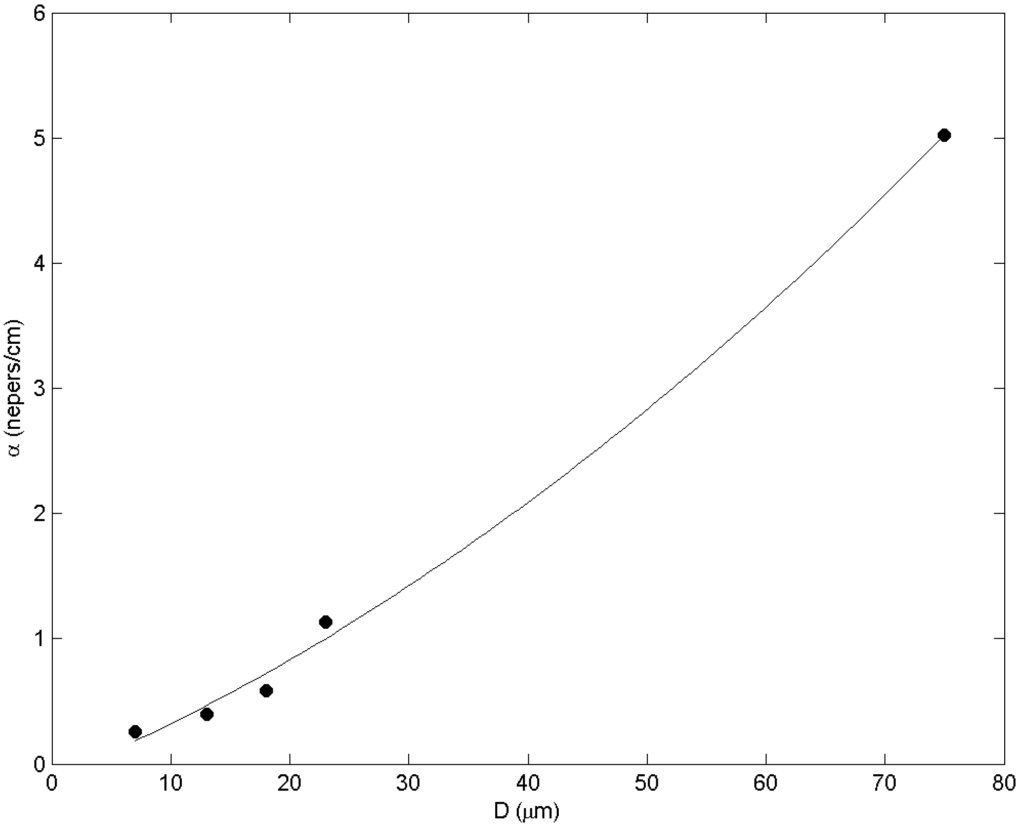

Fig. 4.16. Attenuation coefficient versus mean grain diameter at a single frequency.

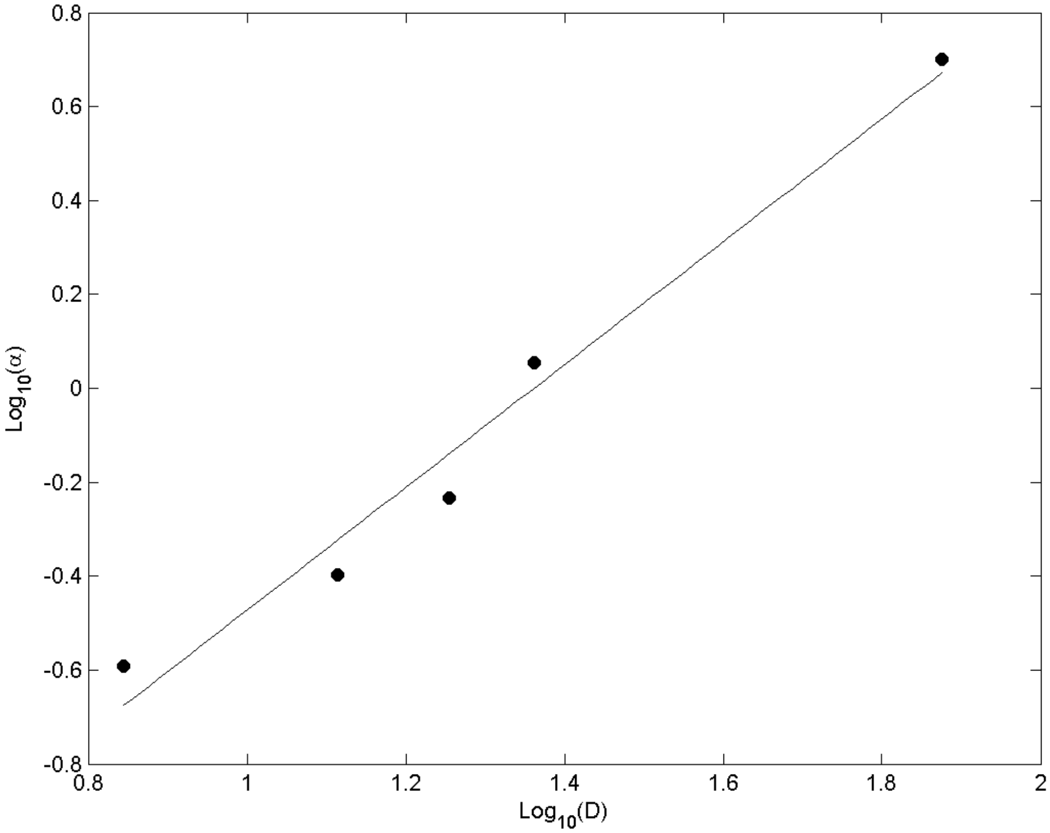

Fig. 4.17. Attenuation coefficient versus mean grain diameter at a single frequency (log10—log10 scale).

Since scattering is related to the ratio of wavelength to mean grain size, the correlation between the attenuation coefficient and mean grain size was considered at fixed wavelengths; therefore, once a common frequency range was selected, each sample's estimated attenuation coefficient was found as a function of wavelength. Each sample's frequency vector was accordingly transformed to a wavelength vector through the relationship $\lambda = \frac{c}{f}$, as was referenced in Chapter 2. Although the discretized frequency increment was identical for all samples' frequency vectors, the discretized wavelengths differed. Differences in wavelength were due to differences in sample wave speeds. For correlation plot generation, these differences were taken into account, as will be explained below.

Once the frequency vector for each sample had been transformed to its corresponding wavelength vector, the solid attenuation coefficient was plotted as a function of wavelength. These curves were smoothed over a selected wavelength range using polyfit.m and then effectively re-digitized by evaluating the polynomials using the same wavelength vector for each sample. This evaluation process ensured that attenuation coefficient estimates could be considered at the same wavelength over all samples. The attenuation coefficient estimates were stored in an array for subsequent generation of correlation plots. Figure 4.18 shows the attenuation coefficient estimates as a function of wavelength for all samples. The wavelength region containing positive-valued estimates is identified with a hashed box. Figure 4.19 provides a magnified view of the positive-valued region. A wavelength region for which the data was fitted with a polynomial is also identified.

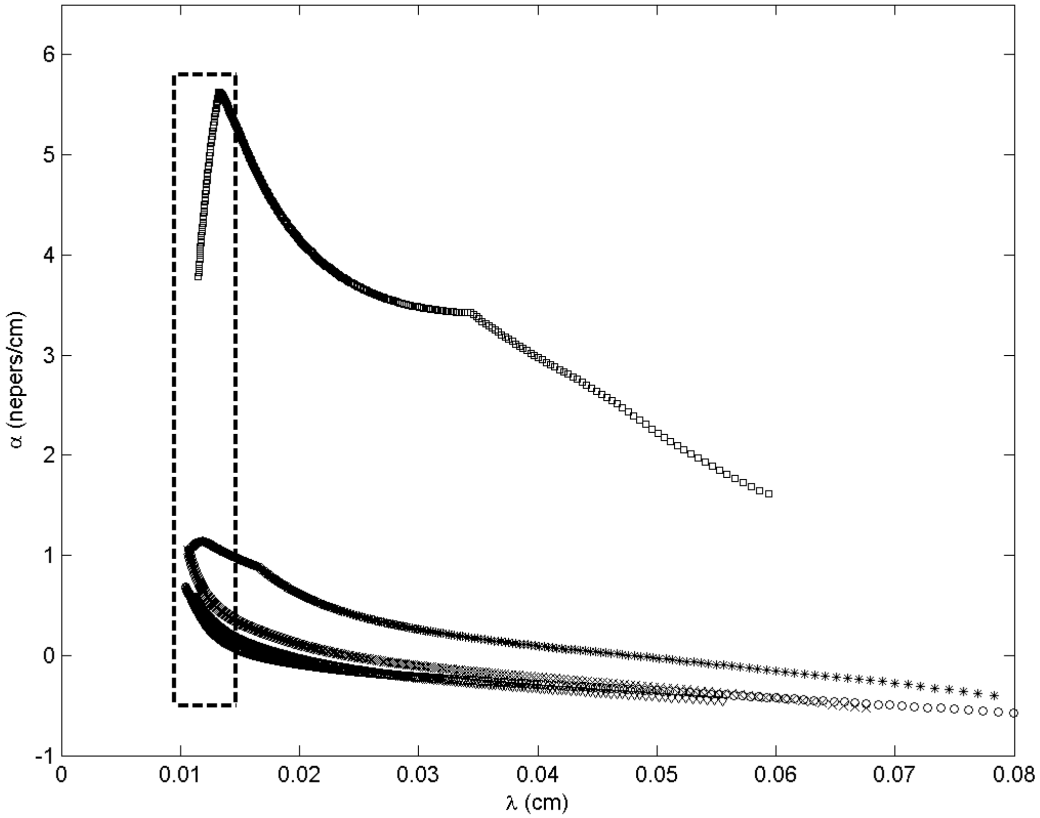

Fig. 4.18. Attenuation coefficient as a function of wavelength for all samples, with positive-valued region identified.

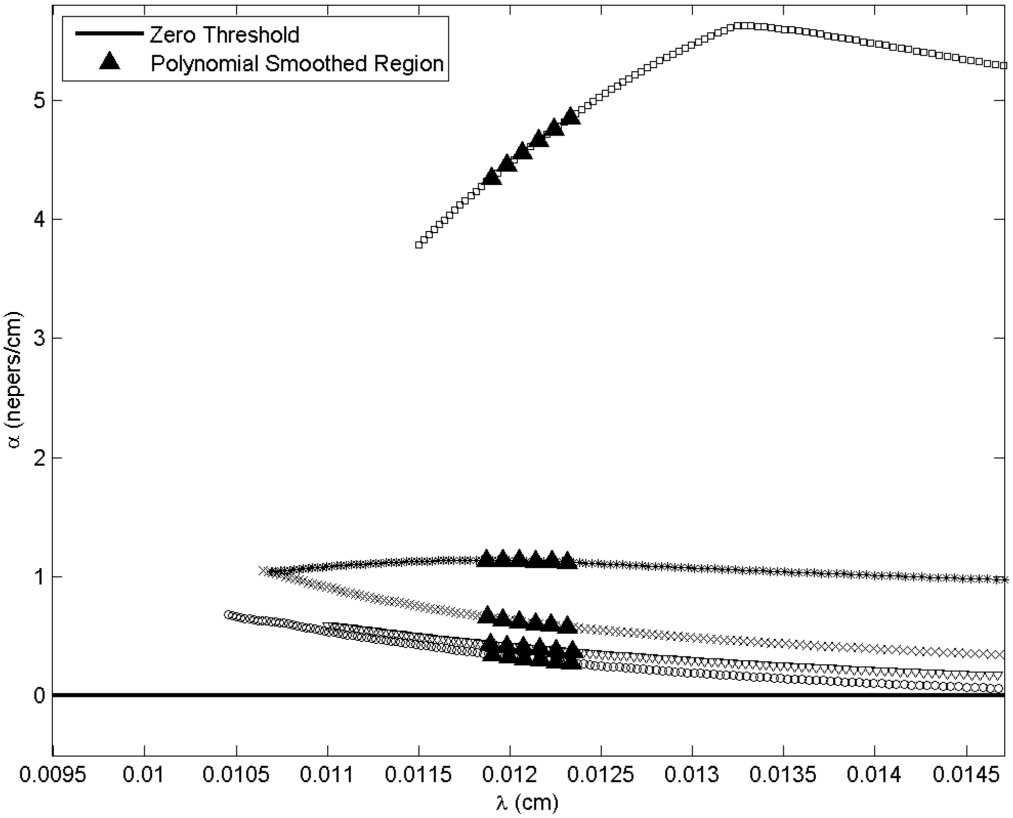

Fig. 4.19. Magnified view of positive-valued region, with a curve fitted region identified.

After storing the attenuation coefficient estimates for all samples within a specified wavelength region, the attenuation coefficient versus mean grain size data was plotted in two formats: $\log_{10}\alpha_s$ versus $\log_{10}D$, as shown in Fig. 4.20, and $\log_{10}D\alpha_s$ versus $\log_{10}\frac{D}{\lambda}$, as shown in Fig. 4.21.

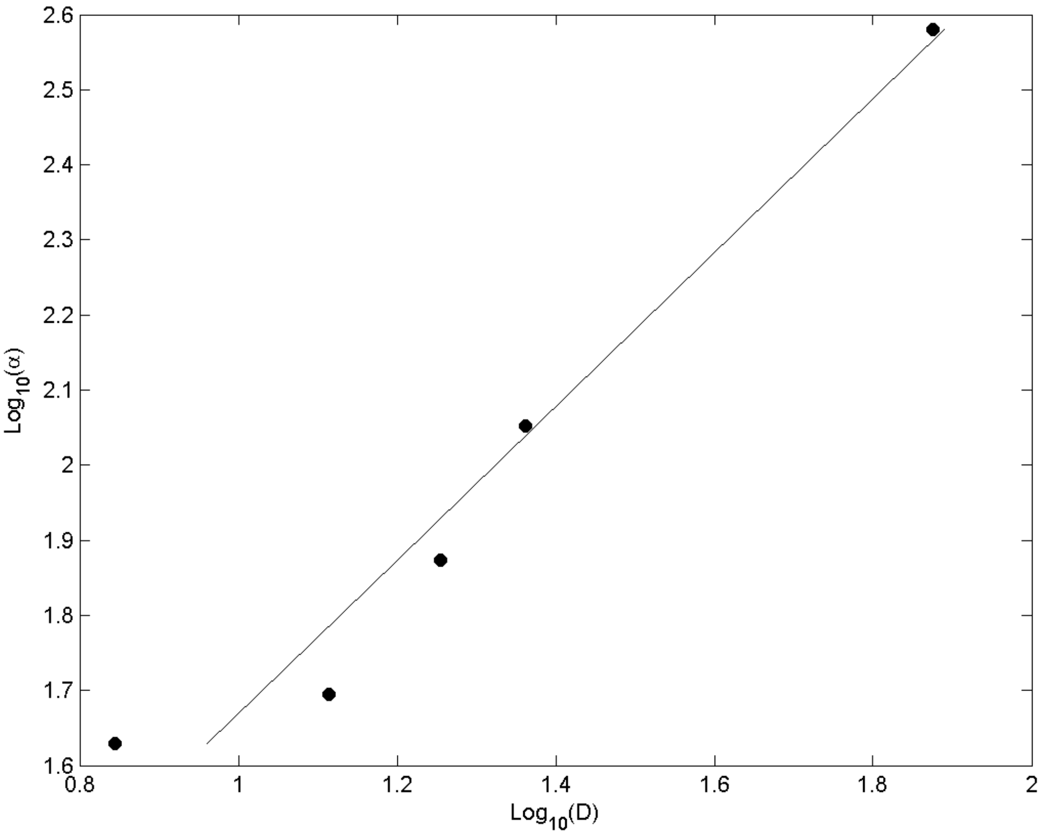

Fig. 4.20. Typical correlation plot generated at a single wavelength.

For the second form (Fig 4.21), the independent variable was parameterized by $\frac{D}{\lambda}$ and the dependent variable was parameterized by $D\alpha$. In past grain diameter estimation work [4, et al.] this parameterization method has been seen to improve the quality of correlation between attenuation and grain diameter for highly populated data sets; however, improved correlation for the sparse data set observed within this research was minimal, if existent at all. Despite there being minimal improvement, all subsequent grain diameter estimation steps were implemented using this second correlation form. An LOO algorithm was employed to obtain grain diameter estimates for each of the 5 samples.

The details concerning this algorithm's methodology and its corresponding grain diameter estimates will be discussed within the next chapter.

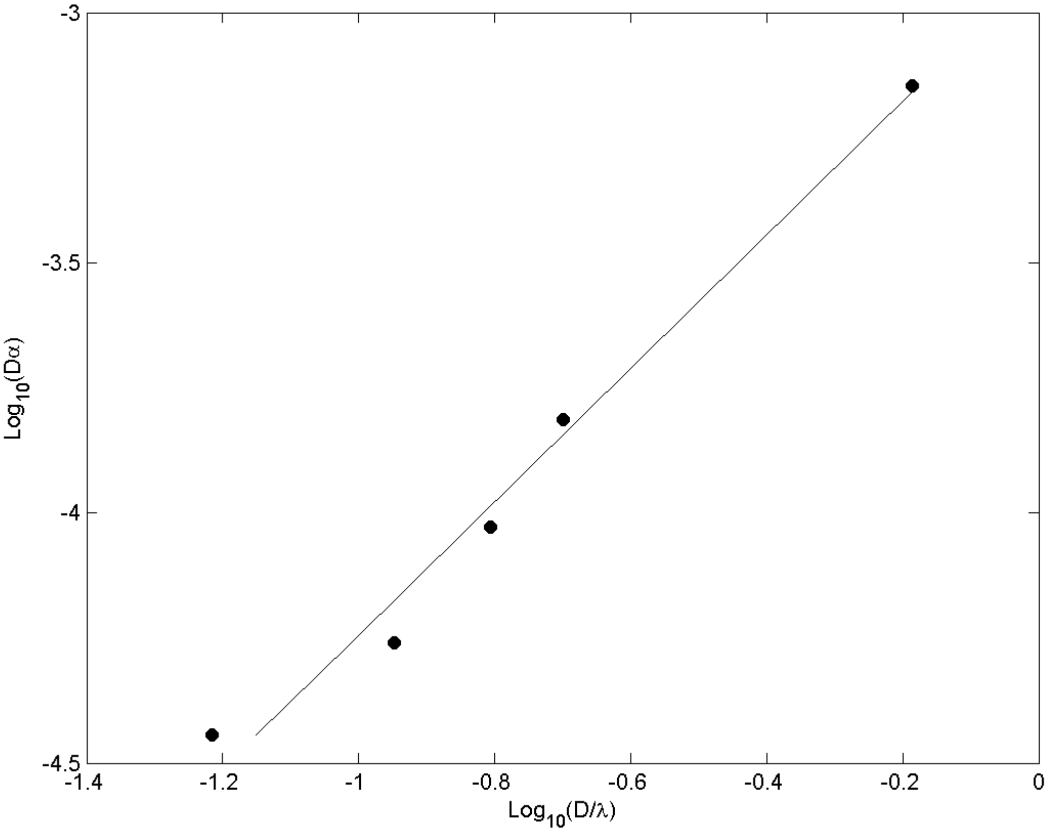

Fig. 4.21. Typical correlation plot generated at a single wavelength (parameterized by $D\alpha$ and D/λ).

CHAPTER 5

Results

Given that the data set observed within this research was sparse, an LOO cross-validation algorithm was employed to maximize the amount of data utilized for grain diameter estimation. Furthermore, this estimation method was advantageous since cross-validation algorithms are less susceptible to over fitting data, as compared to standard linear regression approaches [17, 18]. The estimation error on the samples' grain diameters was treated as the performance metric of the LOO models. It should be noted that for highly populated data sets, other types of cross-validation algorithms are often utilized, as these algorithms are computationally less expensive and are still capable of accurately capturing a data set's behavior [17, 18]. The LOO algorithm implemented within this research is discussed below.

As was mentioned in Chapter 4, a correlation plot was generated at each wavelength within a selected range. To establish mean grain diameter estimates at each wavelength, the LOO algorithm produced predictive models for every correlation plot. Each correlation plot consisted of 5 predictive models, where each model determined a mean grain diameter estimate for a different sample. Each predictive model was developed using 4 of the 5 samples, that is, a linear regression was fit based on data for 4 of the 5 samples with the data for one sample "left out". The sample "left out" was treated as independent data, and its mean grain diameter was estimated via the predictive model. Each estimate was determined by translating the independent sample's $D\alpha$ parameter directly onto the predictive model's linear regression. The shift required to position $D\alpha$ onto the linear regression was purely dependent upon the $\frac{D}{\lambda}$ parameter, that is, data translation only occurred along the $\frac{D}{\lambda}$ axis. The $\frac{D}{\lambda}$ value corresponding to the needed shift was taken as the predicted parameter. By obtaining this parameter's value and having knowledge of the sampled wavelength, the estimated mean grain diameter was determined. Figures 5.1-5.5 show typical LOO models for each sample at a single wavelength. For each model, the independent sample and its corresponding $\frac{D}{\lambda}$ prediction is identified. Table 5.1 provides the measured thickness, alloy type, and mean grain diameter of each sample, as provided by Wieland [6].

Table 5.1. Sample thickness, alloy type, and mean grain diameter.

Sample	**Thickness (cm)**	**Alloy**	**Grain Diameter (μm)**
1	0.149	CuSn6	7
2	0.160	CuZn30	13
3	0.151	CuSn8	18
4	0.153	CuZn30	23
5	0.107	CuZn30	75

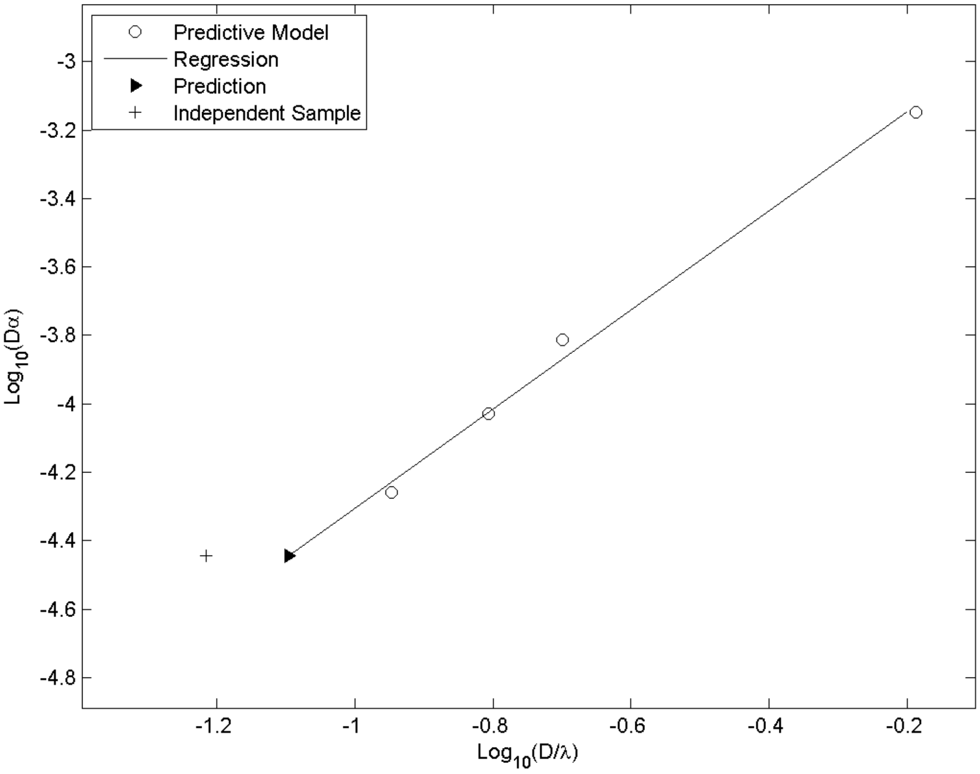

Fig. 5.1. LOO model for sample 1 grain diameter estimation.

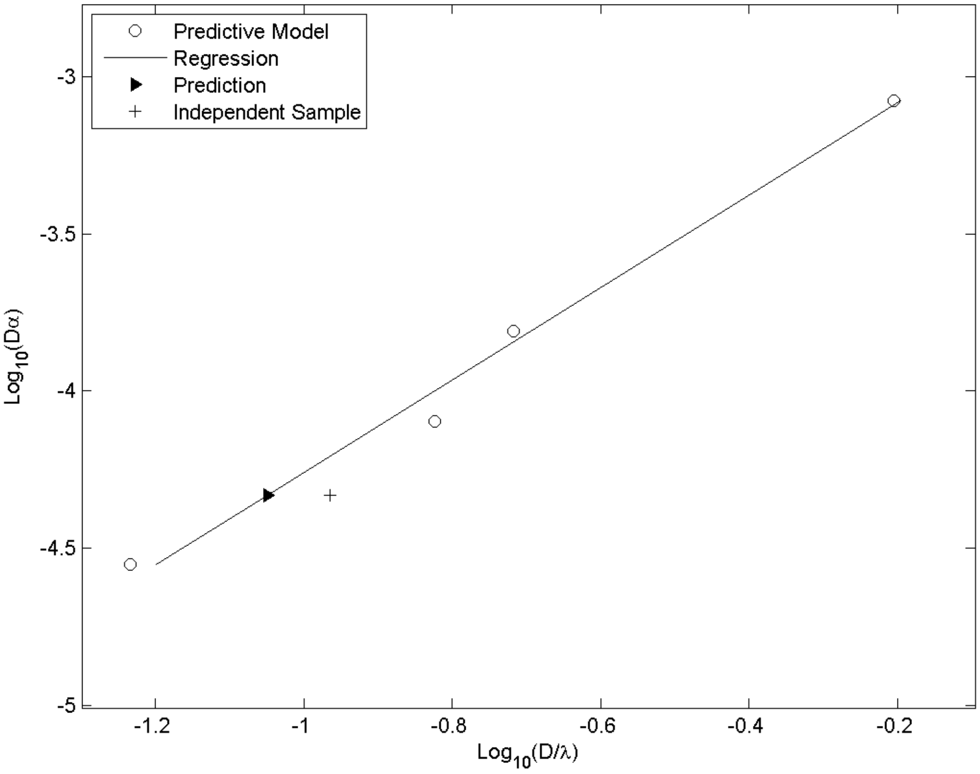

Fig. 5.2. LOO model for sample 2 grain diameter estimation.

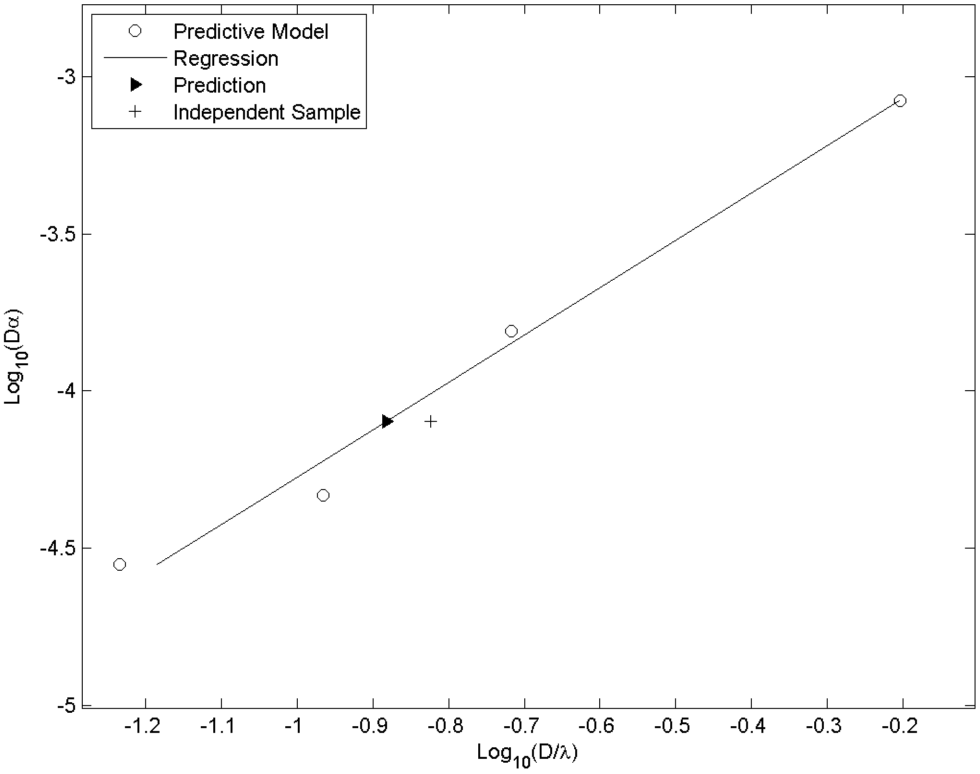

Fig. 5.3. LOO model for sample 3 grain diameter estimation.

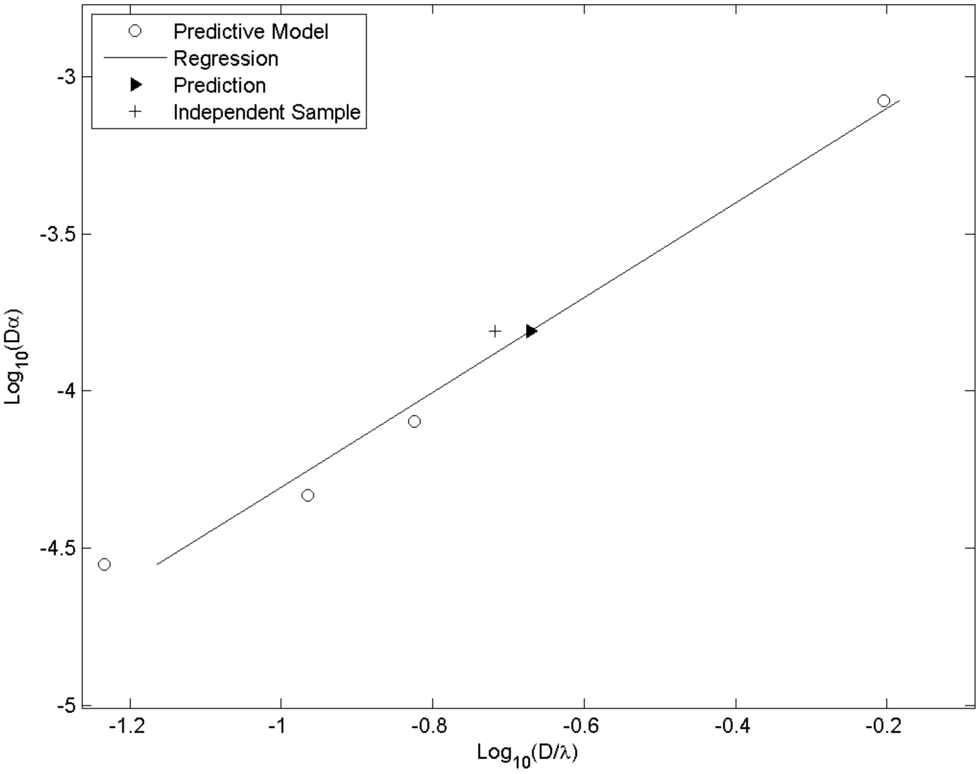

Fig. 5.4. LOO model for sample 4 grain diameter estimation.

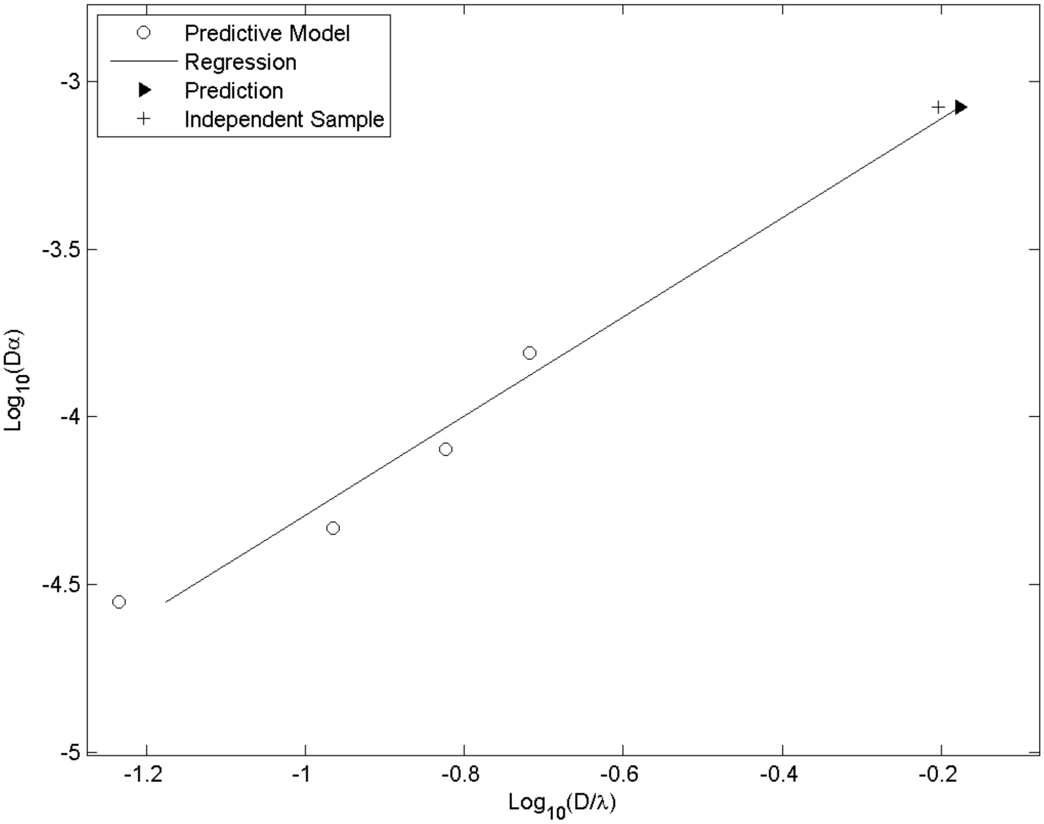

Fig. 5.5. LOO model for sample 5 grain diameter estimation.

Several different wavelength regions were considered using the LOO algorithm, and grain diameter estimates for each sample were determined. This allowed estimation quality to be seen as a function of wavelength. The stated mean grain diameters, as supplied by Wieland were the reference used for determining the accuracy of the estimates. Although the estimation errors did not vary greatly as a function of wavelength, the smallest estimation errors occurred at the smallest wavelengths of the attenuation coefficient data. These estimation errors are reported below.

The maximum estimation error observed at a single wavelength was 22.75%, and the minimum estimation error observed at a single wavelength was 10.38%. The mean estimation error, that is, the estimation error accounting for all sample estimates observed across all wavelengths considered was 16.66%, with a standard deviation of 3.22.

In addition to the LOO approach, a linear regression was fitted to all data comprising each correlation plot, that is, a predictive model was developed by utilizing all 5 samples. The $\frac{D}{\lambda}$ parameter for each sample was determined from the model. The mean estimation error observed with this approach was 9.30%, with a standard deviation of 4.12. Although these error estimates are lower than those found with the LOO algorithm, the LOO models are most likely a better representation of the data's true behavior. This is namely because predictive models defined by an entire data set often tend to over fit the data [17, 18]. Figure 5.6 shows a correlation plot with a predictive model defined by all 5 samples.

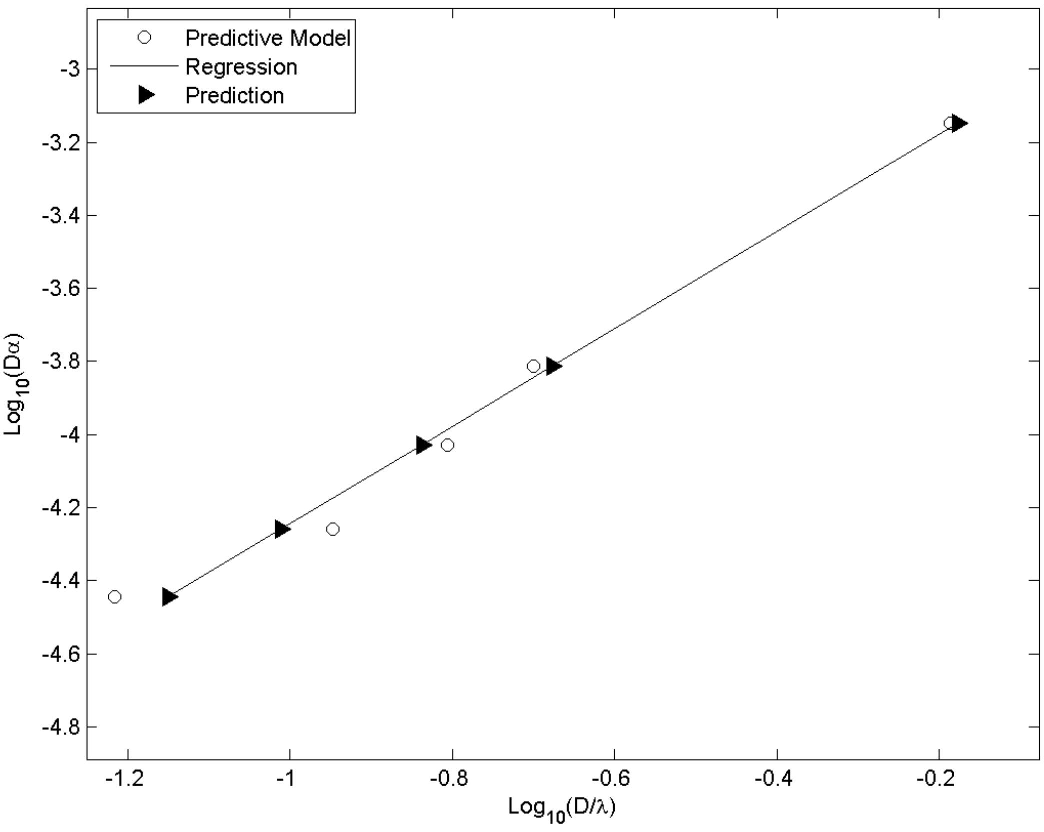

Fig. 5.6. Predictive model comprised of all samples.

CHAPTER 6

Summary and Discussion

The mean grain diameters of 5 thin copper-alloy samples were estimated using ultrasonic attenuation coefficient data acquired in a water immersion, pulse-echo testing mode. Each sample varied in composition, grain diameter, and thickness. Ultrasonic signals for each sample were acquired using axial scans. Signal processing software was developed for attenuation coefficient estimation. Attenuation coefficients were estimated using the magnitude spectra of the front surface reflection and the 1st, 5th, and 6th back surface reflections. Each interface reflection's magnitude spectrum was corrected for beam field diffraction, water attenuation, and reflection and transmission effects. Experimental diffraction correction accounted for changes in beam field diffraction at each interface reflection, and a water attenuation filter accounted for changes in water attenuation at each axial measurement position. Reflection and transmission coefficients were estimated from the experimentally calculated sample wave speeds. The thin profile of each sample presented considerable difficulties for attenuation detection at lower frequencies (long wavelength) where the attenuation is lower; however, a strong correlation between the attenuation coefficient and mean grain diameter was evident at the higher frequencies (short wavelength) where the attenuation was higher. A Leave-One-Out cross-validation algorithm generated correlation models required for grain diameter estimation. Grain diameter estimates were established for each sample and showed promising results. The mean estimation error was 16.66 %, with a standard deviation of 3.22.

These results validated the capability to establish initial grain diameter estimates on thin copper-alloys using the attenuation coefficient estimation method documented within this work. Due to the stochastic nature of a material’s grain structure, future research should focus on evaluating the repeatability and robustness of this documented approach, building correlation models comprised of a far greater number of samples. This will require a much larger number of material samples. Accuracy and repeatability of the estimation approach could be assessed within a given alloy type and across alloys, and at fixed thickness and across varying thickness samples. The utility of this approach for grain size estimation in a manufacturing environment could then be evaluated.

References

1. P.P. Nanekar and B.K. Shah, “Characterization of material properties by ultrasonics,” *BARC Newsletter*, 2003, no. 249, pp. 25-38.

2. H. Ogi, M. Hirao, and T. Honda, “Ultrasonic attenuation and grain-size evaluation using electromagnetic acoustic resonance,” *The Journal of the Acoustical Society of America*, vol. 98, no. 1, pp. 458-464.

3. E.P. Papadakis, “Ultrasonic attenuation caused by scattering in polycrystalline metals,” *The Journal of the Acoustical Society of America,* vol. 37, no. 4, pp. 711-717.

4. L.R. Botvina, L.J. Fradkin, B. Bridge, “A new method for assessing the mean grain size of polycrystalline materials using ultrasonic NDE,” *Journal of Materials Science*, vol. 35, pp. 4673-4683.

5. J. Saniie, N. M. Bilgutay, “Quantitative grain size evaluation using ultrasonic backscattered echoes,” *The Journal of the Acoustical Society of America,* vol. 80, no. 6, pp. 1816-1824.

6. Cu-alloys samples were supplied by Wieland-Werke AG, Ulm, Germany.

7. A.W. Kinzie, *Simultaneous Estimation of Ultrasonic Properties*, MS thesis, University of Missouri, 2005.

8. B.A. Rinker, *A Single-sided Access Simultaneous Solution for Acoustic Wave Speed and Sample Thickness for Isotropic Materials of Plate-type Geometry*, MS thesis, University of Missouri, 2006.

9. H.F. Pollard, *Sound Waves in Solids,* Pion Limited, London, 1977.

10. S.P. Neal, Private Communication, University of Missouri, 2010.

11. T.P. Lerch, R. Cepel, and S.P. Neal, “Attenuation coefficient estimation using experimental diffraction corrections with multiple interface reflections,” *Ultrasonics*, vol. 44, pp. 83-92, 2006.

12. R. Cepel, LabVIEW® program, University of Missouri, 2000.

13. L.E. Kinsler, A.R. Frey, A.B. Coppens, and J.V. Sanders, *Fundamentals of Acoustics*, Wiley and Sons, NY, 2000.

14. J.M.M. Pinkerton, "The absorption of ultrasonic waves in liquids and its relation to molecular constitution," *Proc. Phys. Soc. London*, Sec. B, vol. 62 (1949) 129-141.

15. S.P. Neal, MATLAB® program, University of Missouri, 2010.

16. T.P. Lerch, and S.P. Neal, "Attenuation coefficient estimation using equal diffraction points with multiple interface reflections," *Review of Progress in Quantitative Nondestructive Evaluation,* American Institute of Physics, vol. 22b, pp. 1759-1766, New York, 2003.

17. A.W. Moore, "Cross-validation for detecting and preventing overfitting," Carnegie Mellon University, http://www.cs.cmu.edu/~awm/tutorials, (16 Nov. 2011).

18. R. Gutierrez-Osuna, "Validation," Wright State University, http://www.wright.edu, (16 Nov. 2011).